

Multi-wavelength study of X-ray luminous clusters at $z \sim 0.3$

I. Star-formation activity of cluster galaxies[★]

F. G. Braglia^{1,3}, D. Pierini¹, A. Biviano², and H. Böhringer¹

¹ Max-Planck-Institut für extraterrestrische Physik, Giessenbachstrasse 1, 85748 Garching bei München, Germany
e-mail: [fbraglia;dpierini;hxb]@mpe.mpg.de

² INAF – Osservatorio Astronomico di Trieste, via G. B. Tiepolo 11, 34143 Trieste, Italy
e-mail: biviano@oats.inaf.it

³ Department of Physics and Astronomy, University of British Columbia, 6224 Agricultural Road, V6T 1Z1 Vancouver BC, Canada
e-mail: fbraglia@phas.ubc.ca

Received 23 December 2008 / Accepted 4 February 2009

ABSTRACT

Context. The current paradigm of cosmic formation and evolution of galaxy clusters foresees growth mostly through merging. Galaxies in the infall region or in the core of a cluster undergo transformations owing to different environmental stresses.

Aims. For two X-ray luminous clusters at redshift $z \sim 0.3$ with opposite X-ray morphologies (i.e., dynamical states), RXCJ 0014.3-3022 and RXCJ 2308.3-0211, we assess differences in galaxy populations as a function of cluster topography. This is a pilot study for the joint X-ray and optical analysis of the REFLEX-DXL cluster sample.

Methods. Cluster large-scale structure and substructure are determined from the combined photometry in the B , V , and R bands, and from multi-object optical spectroscopy at low resolution. Photometric redshifts and broad-band optical colours are determined. A spectral index analysis is performed, based on the [O II]($\lambda\lambda 3726, 3728 \text{ \AA}$) and H_β ($\lambda 4102 \text{ \AA}$) features, and the D4000 break, which are available for more than 100 member galaxies per cluster. Additional far-ultraviolet (FUV) photometry is retrieved from the GALEX archive. Combination of spectral indices and FUV-optical colours provides a picture of the star-formation history in galaxies.

Results. In spite of the potential presence of a small fraction of galaxies with obscured star-formation activity, the average star-formation history of cluster members is found to depend on clustercentric distance and, more interestingly, on cluster substructure. The core regions of both clusters mainly host galaxies dominated by old, passively evolving stellar populations, which define the same red sequence in a $(B - R)$ colour– R magnitude diagram. However, a sharp increase in star-formation activity is found along two clearly evident filamentary structures of the merging cluster RXCJ 0014.3-3022, out to its virial radius and beyond. It is produced by luminous (i.e., $L_R \geq L_R^*$) and sub- L^* galaxies. In contrast, the regular cool-core cluster RXCJ 2308.3-0211 mostly hosts galaxies that either populate the red sequence or are becoming more passive. This finding holds out to the cluster virial radius, and also for its immediate large-scale environment.

Conclusions. These results suggest the existence of a correspondence between assembly state and overall age of the stellar populations of galaxies inside the virialized region and in the surrounding large-scale structure of massive clusters at $z \sim 0.3$.

Key words. galaxies: clusters: general – galaxies: evolution – galaxies: stellar content – cosmology: observations – X-rays: galaxies: clusters

1. Introduction

X-ray emitting clusters signpost the largest amounts and concentrations of (cold) dark matter (CDM) in bound systems. At the same time, they contain large samples of coeval galaxies within a well defined environment. This enables to study how galaxy properties, such as star-formation rate (SFR), vary as a function of environment and local density.

Detailed numerical simulations confirm that clusters tend to form at the intersection of filaments and sheets in the evolving large-scale structure of the Universe. Over time, matter begins to fall along such structures and accretes onto clusters. The infall pattern is not random: paths show a correlation in time and are almost stable, so that matter is channelled into a cluster through filamentary structures with persistent geometry. Matter does not

accrete in a steady and continuous way, but in clumps and bound structures, which can be identified as infalling groups of galaxies or less massive clusters (Colberg et al. 1999).

The existence of extended filamentary structures and voids in the large-scale spatial distribution of local galaxies has been known since the advent of redshift surveys (e.g. Gregory & Thompson 1978; Davis et al. 1982). Deep X-ray imaging of emission from hot (10^5 – 10^7 K) gas and the analysis of the two-dimensional distribution of galaxies at the same (photometric or spectroscopic) redshift of a cluster have extended the detection of filamentary networks around clusters to redshifts of $z \sim 0.6$ (e.g. Kull & Böhringer 1999; Scharf et al. 2000; Kodama et al. 2001; Zappacosta et al. 2002; Durret et al. 2003; Ebeling et al. 2004; Dietrich et al. 2005).

The galaxy populations in cluster-feeding filaments can be expected to differ from those in the cluster main body or in the adjacent field, since filaments are an environment of transition between the low and extremely high density regimes.

[★] Tables 9 and 10 are only available in electronic form at the CDS via anonymous ftp to cdsarc.u-strasbg.fr (130.79.128.5) or via <http://cdsweb.u-strasbg.fr/cgi-bin/qcat?J/A+A/500/947>

Consistently, observations have revealed a clear correlation between galaxy morphology or SFR and local density or cluster-centric distance (Dressler et al. 1980, 1997; Whitmore et al. 1993; Balogh et al. 1997). The past and present star-formation activities of galaxies appear to differ between low and high density environments already at intermediate redshifts (Abraham et al. 1996; Morris et al. 1998; Poggianti et al. 2006). From a spectral index analysis of galaxies in 15 X-ray luminous clusters at $0.18 < z < 0.55$, Balogh et al. (1999) concluded that the increase in the observed star-formation activity towards the outer regions of clusters is consistent with an age sequence: galaxies in cluster outskirts have experienced star-formation episodes more recently than galaxies in cluster cores. Their interpretation was that the truncation of star-formation in cluster galaxies may largely be a gradual process, perhaps due to the exhaustion of gas in galaxy discs over fairly long timescales. In this case, differential evolution may result because field galaxies can refuel their discs with gas from extended halos, thus regenerating star-formation, while cluster galaxies may have lost such gaseous halos as well as their dark matter ones (cf. Halkola et al. 2007), and continue to evolve passively.

Combining X-ray and optical observations, Böhringer et al. (2006) and Braglia et al. (2007, hereafter referred to as BPB07) provided evidence of two filaments extending out from the main body of the cluster RXCJ 0014.3–3022 (alias Abell 2744, AC 118) and beyond its virial radius. This is one of the 13 clusters at $z = 0.27–0.31$ of X-ray luminosity higher than $10^{45} \text{ erg s}^{-1} \text{ cm}^{-2}$, selected from the ROSAT-ESO Flux Limited X-ray (REFLEX) cluster survey (Böhringer et al. 2001a) and observed with XMM-Newton, which constitute the Distant X-ray Luminous (DXL) cluster sample (Zhang et al. 2006). It is also a major-merger system (e.g. Boschini et al. 2006) and a “Butcher-Oemler” cluster (Butcher & Oemler 1978a,b, 1984). The blue galaxies in the cluster core, which are more abundant than in present-day massive clusters, are mostly systems involved in major mergers but sub- L^* even in this brightened phase; in their faded state they appear destined to become dwarfs (Couch et al. 1998). BPB07 also found evidence of luminous galaxies along the two filaments exhibiting an enhanced star-formation activity with respect to their counterparts in the field.

More recent studies seem to confirm the increase in star-formation activity along filaments in the outskirts of clusters. For instance, Fadda et al. (2008) reported the presence of twice as many dusty starbursts along two filamentary structures connecting the clusters Abell 1770 and Abell 1763 ($z = 0.23$) as in other cluster regions. Furthermore, Porter et al. (2008) detected a significant enhancement of star-formation, mostly in dwarf galaxies ($M_B > -20$), in a sample of 52 supercluster-scale filaments of galaxies joining pairs of rich clusters of galaxies within the 2-degree Field Redshift Survey region. This work consolidates a similar result obtained for the Pisces-Cetus Supercluster filaments (Porter & Raychaudhury 2007).

The presence of both dwarf and giant galaxies with enhanced SFR and the wealth of available data make the merging cluster RXCJ 0014.3–3022 an interesting laboratory for studying how different physical processes affect galaxy evolution in different cluster environments. To better understand the importance of substructure on star-formation activity in cluster galaxies, we investigate the DXL cluster RXCJ 2308.3–0211 (alias Abell 2537), a cool-core (and thus relaxed) system, in addition to RXCJ 0014.3–3022. The analysis presented here shows the power of combining X-ray observations, wide-field optical imaging, and multi-object spectroscopy in such a study (see also Böhringer et al. 2001b, 2006, 2007; BPB07; Pierini et al. 2008).

Results from a similar analysis applied to the entire REFLEX-DXL sample will be presented in future papers of this series.

This first paper presents in detail the data reduction and analysis techniques, in addition to the results obtained for RXCJ 0014.3–3022 ($z = 0.3068$) and RXCJ 2308.3–0211 ($z = 0.2966$). It is organised as follows. Section 2 provides information about the data quality and reduction, whereas Sect. 3 describes the construction of the photometric and spectroscopic catalogues, and the results obtained from an analysis of the two cluster morphologies and a spectral index analysis for a representative sample of cluster galaxies. A comprehensive discussion follows (Sect. 4), and our conclusions are summarised in Sect. 5.

Hereafter, we adopt a Λ CDM cosmology where $\Omega_m = 0.3$, $\Omega_\Lambda = 0.7$, and $h_{70} = H_0/70 \text{ km s}^{-1} \text{ Mpc}^{-1} = 1$. At the average cluster redshift, 1 arcmin corresponds to 0.267 Mpc.

2. Data: description and reduction

2.1. X-ray imaging

RXCJ 0014–3022 and RXCJ 2308.3–0211 were observed with XMM-Newton in AO-1 and AO-3 as part of the REFLEX-DXL cluster sample (Zhang et al. 2006). Total exposure times were equal to 18.3 and 12 ks, respectively. Observations were performed with thin filter for the three EPIC detectors: MOS data were collected in Full Frame (FF) mode, while *pn* data were taken in Extended Full Frame (EFF) in AO-1 and FF mode in AO-3, respectively. For *pn*, the fractions of out-of-time (OOT) effect are 2.32% and 6.30% for the EFF mode and FF mode, respectively. An OOT event file is created and used to remove statistically the OOT effect. We refer the reader to Zhang et al. (2006) for the entire description of the data reduction. Here it is important to say that RXCJ 0014–3022 and RXCJ 2308.3–0211 have bolometric luminosities equal to $2.12(\pm 0.17) \times 10^{45} \text{ erg s}^{-1}$ and $1.20(\pm 0.13) \times 10^{45} \text{ erg s}^{-1}$, respectively. Furthermore, they were classified as offset centre and single objects, respectively, according to the classification of the dynamical state based on X-ray imaging (Jones & Forman 1992). This corresponds to the different nature of the two clusters, one being a merging systems, the other a regular, centrally peaked, cool-core cluster (Zhang et al. 2006, and references therein).

2.2. Multi-object spectroscopy

Spectroscopic observations in regions of the sky encompassing RXCJ 0014.3–3022 and RXCJ 2308.3–0211 were performed on August 14–16, 2004 (4.4 h per cluster) as part of the ESO Large Program 169.A-0595 (PI: Böhringer), carried out in ESO GO time in visitor and service modes. This program aimed to observe the largest possible number of member galaxies lying in a wide region centred at the X-ray centroid of a cluster, for 7 of the 13 DXL clusters. This was achieved by multi-object spectroscopy (MOS) in low resolution mode with VIMOS (Visible Multi-Object Spectrograph), which is mounted at the Nasmyth focus B of VLT-UT3 *Melipal* at Paranal Observatory (ESO), Chile. VIMOS is a wide-field imager and multi-object spectrograph operating in the visible (from 3600 to 10 000 Å). It is made of four identical arms, each with a field of view (FOV) of $7' \times 8'$ and a $0.205''$ pixel size, separated by a gap between each quadrant of $\sim 2'$. Thus, the total FOV is $4 \times 7' \times 8'$. Each arm is equipped with 6 grisms, providing a spectral resolution ranging from 200 (low) to 2500 (high), and one EEV CCD $4k \times 2k$.

The selection of targets for spectroscopy followed a strict luminosity criterion, in order to minimise the probability of bias on future results about cluster dynamics, galaxy populations, and star-formation activity, which can potentially be introduced by additional colour selection. We selected *I*-band for pre-imaging, since it provides the closest approximation of a selection in terms of stellar mass among the optical bands available for VIMOS. In fact, *I*-band probes emission from stellar populations mostly older than 1–2 Gyr at $z \sim 0.3$, which are least affected by recent episodes of star-formation activity. As a consequence, different environments are sampled with equal probability, given the well-known existence of a correlation between density and star-formation activity (Dressler 1980; Whitmore et al. 1993).

Pre-imaging was executed by adopting three different pointings with two ditherings of $15''$ each, in order to allow the most complete coverage of the cluster central region, a good coverage of the cluster outskirts and sufficient overlap for the cross-shaped gaps between the CCDs. The three pointings were aligned in the E-W direction and partly overlapped, providing a total continuous coverage of about $34'$ in RA and $20'$ in Dec. This corresponds to an uninterrupted coverage of the cluster out to $2.7 h_{70}^{-1}$ Mpc and a fairly good coverage of the outskirts out to $4.6 h_{70}^{-1}$ Mpc at the cluster redshift (see Fig. 1).

An 8-min exposure time per pointing, coupled with the photon collecting area of the 8-m class VLT, enabled us to sample completely galaxies to $I \sim 22.5$, which corresponds to about $M_I^* + 2$ for the RXCJ 0014.3-3022 core (see Couch et al. 1998), where M_I^* is the absolute magnitude corresponding to the characteristic luminosity (L^*) of the *I*-band galaxy luminosity function (LF, see Schechter 1976). Detection and identification of galaxies, together with extraction of photometry, were accomplished by using *SExtractor* (Bertin & Arnouts 1996). Galaxies with $17 \leq I \leq 19$ or $19 < I \leq 21.5$ were successively classified as bright or faint, respectively. Two VIMOS masks per pointing were prepared using the VMMPs tool from ESO¹, one for the bright objects and one for the faint ones. The former were flagged as compulsory targets, whereas the latter were selected as targets by the software, with the only requirement that the number of objects per mask was maximised. This approach allowed spectra to be obtained for most of the bright galaxies without biasing the overall target selection; at the same time, the LF of cluster galaxies was sampled across L^* .

As for MOS observations, a minimum value of the signal-to-noise ratio (S/N) equal to 10 (5) was required for bright (faint) galaxies, which set the total exposure time to be equal to 6 (82) min. This time was divided in three exposures per mask, a total of six masks (three for bright objects and three for faint ones) covering the region containing each cluster. Mask were designed for the LR-Blue grism, which provides a spectral coverage from 3700 to 6700 Å (observed frame) at a spectral resolution of about 200 for a $1''$ slit width, and does not suffer from fringing. For objects at $z = 0.3$, the wavelength range 2830–5130 Å was mapped, which contains important spectral features that were expected to be detected on the basis of the S/N requirements. Among them, the most relevant are the [OII], [OIII], H_β , H_γ , and H_δ emission lines, the CaII_{H+K} absorption lines, and the 4000 Å break. These spectral features are extremely valuable for determining spectroscopic redshifts to $z \sim 0.8$ and increase their accuracy beyond that provided by the set-up. Because of the multiplexing capability of the LR-Blue grism, which enables to stack up to 4 spectra along the spectral dispersion direction, approximately 150–200 spectra per mask

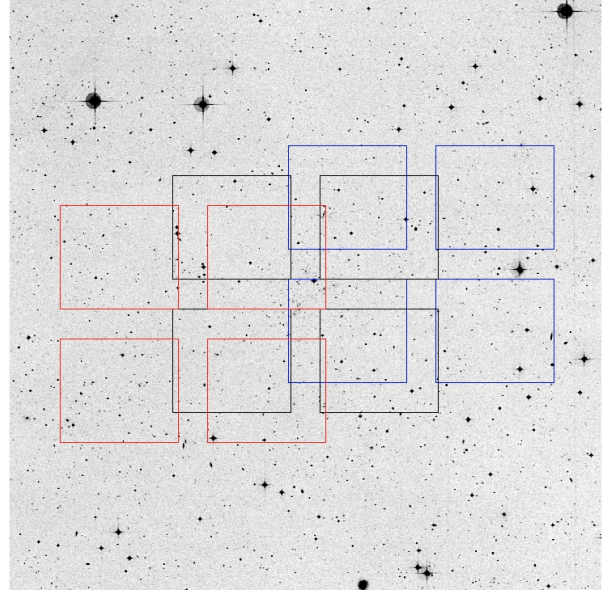


Fig. 1. Mask setup for the VIMOS observations of RXCJ 0014.3-3022, overlaid onto the corresponding DSS field. Each set of four boxes with the same colour represents one pointing; the VIMOS quadrants are aligned in the EW direction.

were collected, depending on the brightness and position of the targets. Slits across individual targets were designed to include a region of empty sky of $3''$ length, providing a suitable sky subtraction.

Data from the MOS observations previously described were reduced mainly using the dedicated software VIPGI², which is a complete data reduction environment developed specifically to handle and reduce data from imaging, MOS and integral-field-unit spectroscopy with VIMOS. Its capabilities and quality have been tested during the reduction of many tens of thousands spectra from the VVDS, and are thoroughly explained in the aforementioned publications. In addition to bias and flat-field correction, multiplex spectra identification, sky subtraction, spectral reduction, and wavelength calibration, VIPGI is capable of data editing and redshift evaluation based on single- and multiple-line fitting, after manual selection of candidate lines to be matched with available line catalogues. Data reduction followed the standard approach, fully described in the VIPGI manual and in Scodreggio et al. (2005). A master bias frame was obtained, where possible, by combining all the available bias frames from the night; rejection of overscan areas and/or bad pixels was performed by a standard 3σ clipping procedure applied throughout the data cube defined by the bias frames. In particular, the adjustment of initial guesses for wavelength calibration was usually fairly quick: a check of the line catalogue of the arcs always produced good agreement with the positions of features in the arc spectra, so only small shifts of 1 to 3 pixels (i.e., about 4 to 15 Å at the resolution of the LR-Blue grism) were introduced as a correction. None of the quadrants was found to be tilted or rotated. The complete adjustment of the calibration arcs was usually performed with a small shift of less than 5 pixels (i.e., about 20 Å) in the dispersion direction. Also spectra detection, based on the adjusted arc calibration, was performed using

² VIPGI (VIMOS Interactive Pipeline and Graphical Interface, Scodreggio et al. 2005) is developed by the VIRMOS Consortium to handle the reduction of the VIMOS data for the VVDS (VIMOS VLT Deep Survey, Le Fèvre et al. 2005).

¹ <http://www.eso.org/observing/p2pp/OSS/VMMPs>

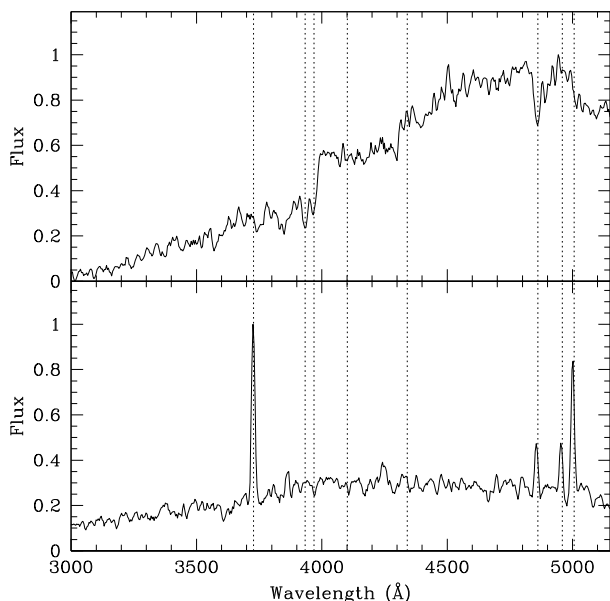


Fig. 2. Examples of VIMOS spectra (rest frame, normalised) for two members of RXCJ 2308.3-0211, with typical spectral features marked. *Top*: an elliptical galaxy, with Ca II_{H+K} ($\lambda\lambda$ 3933.7, 3968.5 Å) absorption lines and H β (λ 4861.3 Å) feature in absorption. *Bottom*: an emission-line galaxy, with [O III] (λ 3727.5 Å), H β , and [O III] ($\lambda\lambda$ 4958.9, 5006.8 Å) emission features.

standard parameters. After manual correction of shifted lines slit by slit, the wavelength calibration has a typical rms of ~ 1.5 Å.

As for science spectra, a combined reduction of the three frames per mask was performed with the *Reduce Sequence of Observations* tool of VIPGI. This avoids confusion with noise and residuals from non-optimal bias removal and flat-field correction; in addition, it enables detection of objects that are fainter than expected. The minimum detection level was set to be equal to 3σ for bright and faint targets, where sky subtraction was based on a fit with a 3rd-order polynomial over each single frame instead of using a simple median over the stack of three frames. This procedure was found to provide a more accurate estimation of the sky emission and more robust detections: using a median-based sky subtraction instead, up to 15% of the faint targets could remain undetected. Spectra of individual targets were extracted using Horne’s algorithm (Horne 1986); standard parameters for detection and deblending (i.e., disentangling of multiple spectra falling in the same slit) were used, because they provided a robust extraction. At the end, all spectra were inspected by eye to check if residual sky contamination, hot pixels, ghosts arising from the superposition of different spectral orders, and other artifacts were present, and if all targets had been successfully extracted. In addition, initial values of the S/N were computed for the continuum emission and spectral features.

Spectroscopic redshifts were mainly determined by VIPGI (the EZ³ package, plus software for the manual detection and fit of spectral features). After a pipeline determination for all spectra, individual redshifts were inspected by eye and manual determination was executed in case of a probable misidentification. In general, spectra with initial values of the S/N equal to 4 (at least) in the continuum and higher than 10 for spectral features enabled a clear determination of spectral types, and, thus, provided an unambiguous determination of redshifts. Typically a reliable

spectrum could not be extracted from data of a mean S/N less than 3; the corresponding slits were flagged for removal. Non-detections were used to evaluate the mean spectral noise, which amounts to ~ 20 counts/pixel, the blue spectral region covered by the LR-Blue grism (i.e., $\lambda < 5000$ Å) being slightly noisier than the red one. The faintest, reliably detected spectra have continuum fluxes of between 100 and 500 counts/pixel, depending on the spectral type, and spectral features of high S/N .

2.3. Wide-field imaging

Optical photometry was carried out using the wide-field imager (WFI) mounted at the Cassegrain focus of ESO/MPG-2.2 m telescope at La Silla, Chile. WFI (Baade et al. 1999) is a focal reducer-type mosaic camera consisting of 4×2 CCD chips, each with 2048×4096 pixels and a FOV of $8.12' \times 16.25'$ ($0.238''/\text{pixel}$). Chips are separated by gaps of $23.8''$ and $14.3''$ in the RA and Dec directions, respectively, such that the WFI FOV is $34' \times 33'$, with a filling factor of 95.9%. The data presented here were obtained as part of a program carried out in visitor and service modes (P.I.: Böhringer) during MPG observing time. In particular, observations of RXCJ 0014.3-3022 and RXCJ 2308.3-0211 in the B , V , and R passbands were performed between September 27 and 30, 2000, in photometric conditions. They were divided into sequences of eight dithered sub-exposures. Total exposure times are listed in Table 1. Filter curves can be found in Arnouts et al. (2001) and on the web page of the La Silla Science Operations Team⁴. Standard stars were observed in all the four nights: three Landolt fields (Landolt 1992) were targeted for a total of 16 standard star OBs per filter.

The WFI data were reduced using the data reduction system developed for the ESO Imaging Survey (EIS, Renzini & da Costa 1997) and its associated EIS/MVM image processing library version 1.0.1 (*Alambic*, Vandame 2004). *Alambic* is a publicly available⁵ software designed to automatically transform raw images from single/multi-chip optical/infrared cameras into reduced images for scientific use. In addition to the standard bias-subtraction, flatfield correction, and trimming, the EIS/MVM image processing pipeline performs background estimation, de-fringing (if needed), astrometric calibration, minimisation of chip-to-chip variations in sensitivity, and detection/masking of satellite tracks. All of these steps are described in detail in previous publications (Arnouts et al. 2001; Vandame 2004; Mignano et al. 2007; Pierini et al. 2008), and, thus, are omitted here. However, we note that the astrometric calibration was derived using the GSC2.2 reference catalogue and a distortion model described by a second order polynomial. Its precision is $0.2''$ but the internal accuracy is about 70 mas (see Mignano et al. 2007). Furthermore, we note that the CCD-to-CCD gain variations were corrected using median background values sampled in sub-regions bordering adjacent CCDs, but that no illumination correction was applied. This may lead to relative zero-point offsets from the centre to the borders of the image of up to 10%, according to the *still experimental* method designed by Selman to derive a zero-point correction map (Selman 2004).

Source detection and photometry were based on SExtractor (Bertin & Arnouts 1996) both for standard and science images. Magnitudes were calibrated to the Johnson-Cousins system using Landolt (1992) standard stars whose magnitudes were obtained using a 10 arcsec-wide circular aperture, which proved to

³ <http://cosmos.iasf-milano.inaf.it/pandora/>

⁴ <http://www.la.silla.eso.org/lasilla/sciops/2p2/E2p2M/WFI/filters>

⁵ http://www.eso.org/science/eis/survey_release.html

Table 1. Photometric solutions available in this work.

Passband	ZP	k	CT
B	24.66 ± 0.005	0.22	0.26 ± 0.007
V	24.23 ± 0.006	0.11	-0.15 ± 0.012
R	24.50 ± 0.007	0.07	-0.02 ± 0.015

Column 1 the passband; Cols. 2–4 the zeropoint in the Vega magnitude system (ZP), the extinction coefficient (k), and the colour term (CT) together with their errors. These “best fit” parameters were obtained from a two-parameter fit to about 200 measurements across the WFI field for each passband, the extinction coefficient being fixed.

Table 2. “Definitive” photometric solutions obtained by the 2p2 Telescope Team from observations of standard stars in perfectly photometric nights, where a bunch of standard fields were moved around each chip of WFI.

Passband	ZP	k	CT
B	24.81 ± 0.05	0.22 ± 0.015	0.25 ± 0.01
V	24.15 ± 0.04	0.11 ± 0.01	-0.13 ± 0.01
R	24.47 ± 0.04	0.07 ± 0.01	0.00 ± 0.00

All parameters were fitted simultaneously as free parameters, with good airmass and colour range, and around 300 stars per fit. The table below gives the average solutions over all chips.

be adequate by monitoring the growth curve of all the measured stars. Photometric standards were observed over a rather broad range of airmasses, but science frames were taken at the best airmass per target; so the photometric solutions used to calibrate reduced images were obtained from merging all the measurements of standard stars for each passband. The number of non-saturated Landolt stars per field did not allow independent solutions to be determined for each of the eight chips of WFI. Hence calibration had to rely on solutions based on measurements taken across all chips. Although the EIS data reduction system includes a photometric pipeline for the automatic determination of photometric solutions, these were determined interactively using the *IRAF*⁶ task *fitparams*. This choice allows the interactive rejection of individual measurements, stars, and chips. Photometric solutions with minimum scatter were obtained by a two-parameter linear fit to about 200 photometric points per passband, the extinction coefficient being set equal to that listed in the “definitive” solution obtained by the 2p2 Telescope Team⁷. In general, zero-points and colour terms are consistent with those obtained by the 2p2 Telescope Team or by the ESO DEEP Public Survey (DPS) team (Mignano et al. 2007), as can be seen by comparing Tables 2–4.

As for science images, source extraction and photometry were obtained after matching the BVR images of each target to the worst seeing (1 and 1.3'' *FWHM* for RXCJ 0014.3-3022 and RXCJ 2308.3-0211, respectively), using the *IRAF* task *psf-match*, and taking into account the weight-maps associated with the individual images, produced by *Alambic*. A common configuration file was used to produce three catalogues per target,

⁶ *IRAF* is the Image Reduction and Analysis Facility, a general purpose software system for the reduction and analysis of astronomical data. *IRAF* is written and supported by the *IRAF* programming group at the National Optical Astronomy Observatories (NOAO) in Tucson, Arizona. NOAO is operated by the Association of Universities for Research in Astronomy (AURA), Inc. under cooperative agreement with the National Science Foundation.

⁷ <http://www.ls.eso.org/lasilla/Telescopes/2p2T/E2p2M/WFI/zeropoints/>

Table 3. Median values for all the photometric solutions based on three-parameter fits obtained by the ESO DPS team.

Passband	ZP	k	CT
B	24.58	0.22	0.24
V	24.23	0.19	-0.04
R	24.49	0.08	-0.01

Table 4. Background evaluation results for the different subcatalogues of cluster members, for both clusters.

Catalogue	N. objects	Mean BG	rms
RXCJ0014.3-3022 (all)	3698	32.37	10.31
RXCJ0014.3-3022 (red)	1409	9.70	4.28
RXCJ0014.3-3022 (blue)	2289	21.91	6.90
RXCJ0014.3-3022 (spec.)	190	1.90	3.03
RXCJ2308-0211 (all)	4109	44.72	14.74
RXCJ2308-0211 (red)	2361	23.26	9.52
RXCJ2308-0211 (blue)	1748	20.10	7.52
RXCJ2308-0211 (spec.)	269	1.18	5.01

Values are always given in units of number of galaxies per square Mpc.

a minimum number of trivial adjustments (e.g., seeing, zero-point) being made for individual images. The deepest R -band image was used as the detection image, where sources are defined by an area with a minimum number of 5 pixels above a threshold of 1σ of the background counts. Source photometry in individual passbands was extracted in fixed circular apertures (between 1.2'' and 10'' in diameter) or in flexible elliptical apertures (Kron-like, Kron 1980) with a Kron-factor of 2.5 and a minimum radius of 3.5 pixels. Total magnitudes computed from the latter photometry (Kron-like) are used hereafter. Background subtraction was based on values taken directly from the background map, as obtained from a bi-cubic-spline interpolation, after applying median-filtering to subregions of an image equivalent to 3×3 meshes, the mesh-size being equal to 64 pixels (i.e., 15.2''). Object magnitudes were corrected for Galactic extinction according to the Schlegel et al. (1998) Galactic reddening maps (from *NED*) and converted to the AB system according to the response function of the optical system (see Alcalá et al. 2004). The output catalogues were successively culled of fake sources by hand before photometric redshifts were determined. In addition, stars and galaxies could be safely identified on the basis of their surface brightness profile and optical colours to $R = 21.5$. Fainter than this limit, number counts are dominated by galaxies, so that all detected objects with $R > 21.5$ are assumed to be “bona fide” galaxies.

Depth and quality of the final catalogues were assessed in two ways. Firstly, we compared the number counts of stars securely identified in the R -band image of each cluster with those expected from the model of stellar population synthesis of the Galaxy by Robin et al. (2003) for $R \leq 21.5$. A good agreement between measured and expected values was found within the uncertainties. Secondly, we compared the number counts of galaxies, falling either within the entire mapped region of a cluster or in a low-density subregion (i.e., the “field”, see Sect. 3.3), with the galaxy number counts determined in deep fields (in particular VVDS Deep, McCracken et al. 2003). In general, our galaxy number counts exceed those obtained from observations of deep fields for $R \leq 21.5$, where our galaxies were safely identified (cf. Fig. 3). Unsurprisingly, this is especially true when the entire mapped regions of RXCJ 0014.3-3022 and RXCJ 2308.3-0211 are considered. On the other hand, the number counts of

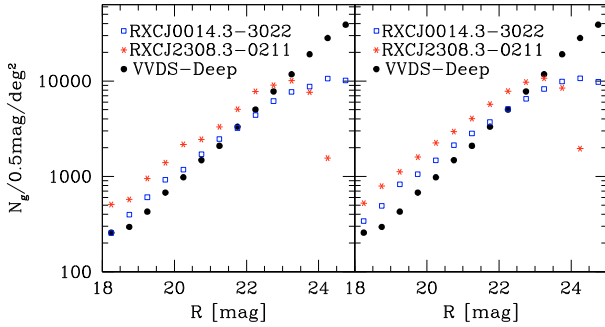


Fig. 3. Comparison of number counts for both clusters and the VVDS-Deep (McCracken et al. 2003). *Left*: number counts in a neighbouring, low density region of each cluster. *Right*: number counts for the entire region of a cluster imaged with WFI.

all galaxies, either within the “field” or the entire mapped region of a cluster, begin to be lower than the galaxy number counts in deep fields at $R = 22$ – 23 . In particular, this deficit amounts to a factor of 2 at around 23.5 R -mag, where the number of background galaxies dominates the number of likely cluster members. Assuming as a completeness limit the magnitude at which the observed counts equal 50% of the expected ones, we thus conclude that our R -band selected catalogues are complete to ~ 23.5 mag.

This holds in spite of the different decrease of number counts in the two cluster regions (see Fig. 3). The different behaviour at $R > 23.5$ mag must be ascribed to a combination of Galactic absorption and seeing. In fact, RXCJ 0014.3-3022 is in a sky region far away from the Galactic Plane and was observed at a typical seeing of $\sim 1''$; in contrast, RXCJ 2308.3-0211 is close to the Galactic Plane and was observed at a typical seeing of $\sim 1.2''$. It is then probable that a higher fraction of objects fainter than ~ 23.5 mag has failed detection in the second region. Consistently, catalogues exhibit comparable numbers of objects with $R \leq 23.5$ mag: 14 409 for RXCJ 0014.3-3022 and 14 820 for RXCJ 2308.3-0211. A Kolmogorov-Smirnov test confirms that number counts for the two complete samples are consistent, the probability of a difference being equal to only 7.1%.

2.4. GALEX UV photometry

In order to constrain more robustly the recent star-formation activity in member galaxies of RXCJ 0014.3-3022 and RXCJ 2308.3-0211, we complemented the optical data with GALEX UV photometry. The GALEX data archive was scanned by means of the MultiMission Archive at Space Telescope Science Institute (MAST⁸). Positions and total magnitudes of galaxies falling in the regions of both clusters were extracted from the All Sky Imaging Survey (GR3 data release). The total UV magnitude of an object was calculated as a weighted mean when multiple detections of the same object were present from overlapping GALEX pointings. In general, cross-identification of GALEX sources with objects in our catalogues was largely unambiguous. When multiple catalogue objects were present within the radius of the GALEX PSF ($6''$ FWHM), the bluest one (i.e., with smaller $(B - R)$ colour) was identified as the counterpart of the UV source. In the absence of GALEX FUV detections, 3σ upper limits to the UV magnitude were computed from the completeness FUV magnitude of the two fields imaged by GALEX.

⁸ <http://galex.stsci.edu>

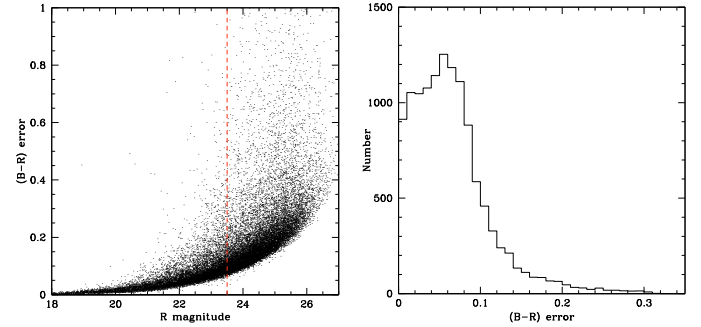


Fig. 4. Photometric quality of WFI data for RXCJ0014.3-3022. *Left*: error on the $(B - R)$ colour as a function of R -band magnitude (R). A vertical dashed line marks the completeness limit $R = 23.5$. *Right*: distribution of errors on $(B - R)$ for the complete sample.

3. Results

3.1. Photometric redshifts

Cluster member galaxies were identified on the basis of photometric or spectroscopic redshifts; two catalogues are built accordingly. In the first case, member galaxies have photo- z 's consistent with the photo- z of the cluster; hence they are “bona fide” members. In this section, we describe how we determine photometric redshifts, estimate their accuracy, and establish cluster membership based on photo- z 's.

Photometric redshifts are obtained by using a prior based on the $(B - R)$ colour⁹, given the limited photometry available. This information is accurate enough only for objects brighter than the completeness limit of the photometric catalogues culled of fake objects and stars brighter than $R = 21.5$ (see Sect. 2.3). This is illustrated by the distribution of the errors on $(B - R)$ as a function of R -band magnitude for the 23 900 objects in the region of RXCJ 0014.3-3022 with $14 < R < 27$ (see Fig. 4). Objects brighter than $R \sim 23.5$ exhibit a typical error in $(B - R)$ of about 0.05 mag; only 248 objects among them (i.e., 0.02% of the complete sample) exhibit errors larger than 0.2 mag, these objects having $21.4 < R \leq 23.5$, with a mean $R = 23.05$.

We successively compiled $(B - R)$ versus R colour-magnitude (CM) diagrams from the complete catalogues of the two clusters, after removing galaxies whose photometry was affected by intervening bright stars, a step that did not have an impact on any of the following results. A visual inspection of both CM diagrams (see Fig. 5) clearly reveals the presence of a red sequence, which exhibits $(B - R) \sim 2.2$ (observed frame). In each case, the red sequence was fitted using an iterative 3σ clipping linear regression algorithm, all objects lying within a distance of $3'$ from X-ray centroid of the cluster and with $17 \leq R \leq 20$ being considered in the first step. The best-fits of the two red sequences are in remarkable agreement, as shown later. Thus, objects in the complete samples of the two clusters are classified as “red” if they are within 3σ of the best-fit equation of the red sequence, or “blue” if their $(B - R)$ colours are bluer than this locus at a significance level of higher than 3σ (see Fig. 5).

This separation provides some guidance for selecting the SED templates used to determine the photometric redshift of each object with the well-tested code *HyperZ* (Bolzonella et al. 2000). Specifically, red galaxies were only fitted using a suite

⁹ At the redshifts of the two clusters, the B and R broad-band filters map, respectively, the rest-frame wavelength ranges 3022–3940 Å and 4247–6045 Å. Hence, these two passbands bracket the 4000 Å break. In addition, B band contains the redshifted emission in the [OII] line.

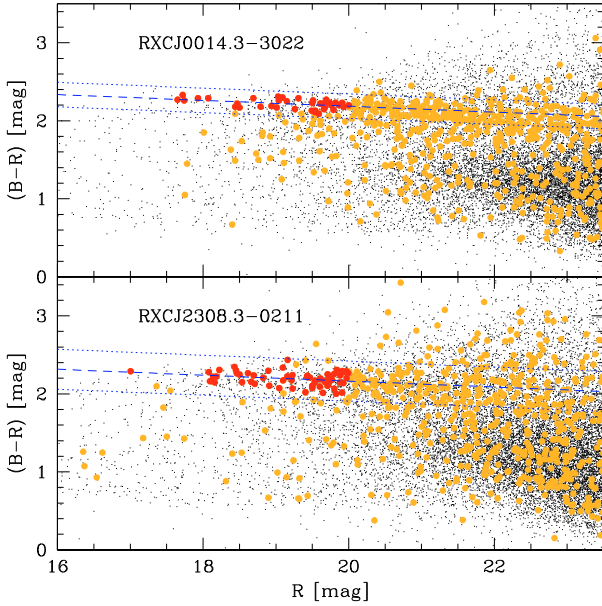


Fig. 5. $(B - R)$ vs. R colour–magnitude diagram (observed frame) for the regions of RXCJ 0014.3-3022 (*upper panel*) and RXCJ 2308.3-0211 (*lower panel*) imaged with WFI. Orange points mark galaxies within $3'$ from the cluster centre: most of them define a red-sequence. Red circles mark galaxies used for fitting the red sequence; this locus is reproduced (dashed line) together with the $\pm 3\sigma$ scatter around it (dotted lines).

of templates for galaxies dominated by old, passively-evolving stellar populations (E and S0 types), whereas blue objects were fitted with a suite of templates for star-forming galaxies (spirals and irregulars). Photometric redshifts were also determined without any prior on colour (i.e., morphology), which provided consistent results. Default synthetic non-evolving templates for E, S0, Sa, Sb, Sc, Sd, and Im galaxies were found to provide the most reliable results. Best-fit solutions from *HyperZ* were trained on spectroscopic redshifts, which provided an rms uncertainty of 0.06 at $z = 0.3$ (see BPB07).

The photometric redshift of a cluster is defined to be the mean of the photo- z 's of its spectroscopic members, as identified in Sect. 3.2. All galaxies with photo- z 's within an interval of $\pm 1\sigma$ (i.e., ± 0.06) centred on z_{phot} are defined as cluster photometric members.

3.1.1. RXCJ 0014.3-3022: photometric members

The CM diagram of the inner region of RXCJ 0014.3-3022 shows that five galaxies populate a narrow bin ($17.6 \leq R \leq 18.1$) at the bright-end of the red sequence. Four of them are part of two visual pairs of BCGs associated with the two X-ray sub-components of the cluster (see Pierini et al. 2008).

Fitting the CM distribution of 41 red-sequence objects, selected with a recursive algorithm, provides:

$$(B - R) = (2.935 \pm 0.238) - (0.037 \pm 0.003) \times R.$$

The rms scatter around this locus is equal to 0.052.

RXCJ 0014.3-3022 has $z_{\text{phot}} = 0.34$ and its bona fide members have a photometric redshift of between 0.28 and 0.4. Its photometric redshift is thus higher than the spectroscopic one ($z = 0.3068$), although the two redshifts are consistent given the large typical uncertainty of photo- z 's. The discrepancy is not driven by contamination from outliers, which is below 10%, or by the overall robustness of the identification of cluster

members (see BPB07), but by blue members, which exhibit higher photo- z 's and a larger scatter with respect to the red members, on average. This is mostly due to the presence of large peculiar velocities (up to 4000 km s^{-1} , see BPB07), which can produce a difference in z of up to ~ 0.02 . The coupling of a relatively large, positive excess in the velocity along the line of sight and the rest-frame wavelength coverage offered by the filter set can increase photo- z 's by about 0.04, but only for blue cluster member galaxies. At the cluster spectroscopic redshift, the redshifted [OII] emission line falls in the red tail of the B filter, and is just shortwards of the blue edge of the V passband, whereas the 4000 \AA break falls in between the two passbands. The former feature characterises star-forming systems and the latter is stronger in old, passively evolving galaxies. Consistently, the photo- z 's of red galaxies (~ 0.32) are in better agreement with the spectroscopic redshift of the cluster.

In conclusion, the catalogue of photometric members of RXCJ 0014.3-3022 comprises 3698 galaxies across a 900 square arcmin-region centred on the X-ray centroid of the cluster, of which 1409 (2289) are classified as red (blue).

3.1.2. RXCJ 2308.3-0211: photometric members

The inner region of RXCJ 2308.3-0211 exhibits a similar red-sequence to that of RXCJ 0014.3-3022, but there are also three interesting differences. First, RXCJ 2308.3-0211 hosts a single BCG, which is brighter than the other red photometric members by at least $\sim 1 R$ -mag. Second, its red sequence is more populated (64 photometric members against 41) and exhibits a 60% larger rms scatter (0.085 against 0.052). Third, red members amount to 57% of the total number in RXCJ 2308.3-0211 compared to 38% in RXCJ 0014.3-3022.

A fit to the red sequence defined by 64 robustly selected objects provides:

$$(B - R) = (2.933 \pm 0.323) - (0.038 \pm 0.003) \times R$$

with a scatter of 0.085. Photometric ($z_{\text{phot}} = 0.29$) and spectroscopic ($z = 0.2966$) redshifts are in excellent agreement for this cluster: thus, galaxies with photo- z 's between 0.23 and 0.35 are identified as members. The catalogue of photometric members of RXCJ 2308.3-0211 contains 4109 objects across a 900 square arcmin-region centred on the X-ray centroid of the cluster, of which 2361 (1748) are classified as red (blue).

3.2. Spectroscopic redshifts

Spectroscopically confirmed members of either cluster were identified from the available spectroscopic catalogues as follows. As a first step, a relatively broad distribution in spectroscopic redshifts was considered, by selecting a range centred on the mean cluster redshift and with a width of 0.05. This is a fairly large value: it corresponds to a velocity range of about 10000 km s^{-1} at $z \sim 0.3$. However, it avoids the “a priori” loss of high-speed cluster members and still enables unambiguous rejection of any other structure present in the foreground/background.

After this selection, cluster membership was estimated by using the biweight estimators introduced by Beers et al. (1990) and successively applied with success in many different studies (e.g. Biviano et al. 1992; Girardi et al. 1993; Adami et al. 1998; Girardi et al. 1998; Biviano et al. 2006). Successively, all objects with peculiar velocities outside the range of $\pm 4000 \text{ km s}^{-1}$ centred on the cluster biweighted redshift were rejected. Interlopers

were then removed following the algorithm of den Hartog & Katgert (1996, see also Katgert et al. 2004), which identifies galaxies unlikely to be bound to the cluster on the basis of their location in projected phase-space. Velocity errors and relativistic correction were applied to the cluster velocity dispersion estimate, as described by Danese et al. (1980). The X-ray centroid of each cluster was used as a reference in these calculations. The application of the overall procedure is discussed in Braglia et al. (2009b, in prep.), and the method was validated by the analysis of clusters extracted from cosmological numerical simulations in Biviano et al. (2006).

Finally, each catalogue of spectroscopic cluster members was cross-correlated with the photometric one, which provided a new catalogue combining photometric and spectroscopic information. All detected spectroscopic targets are brighter than 23.5 R -mag, as expected. For this cross-correlation, the celestial coordinates of spectroscopic members were taken from our pre-imaging. No correction for seeing was introduced since pre-imaging and R -band imaging were executed in similar seeing conditions.

Appendix B provides as online material the complete catalogues of successfully identified non-stellar objects, including cluster members, in both observed fields. The catalogues also contain photometric information from WFI imaging and the spectral indices computed in Sect. 3.4.

3.2.1. RXCJ 0014.3-3022: spectroscopic members

The spectroscopic data reduction produced a total of 545 slits with at least one object in the entire region of RXCJ 0014.3-3022 covered with VIMOS. This corresponds to a total of 872 objects, since 147 slits contained multiple objects (up to 5). Among them, there are 64 serendipitous faint stars. For 262 objects, the S/N is too low for the extraction of a reliable spectrum, so they were flagged as non-detections. Out of the remaining 546 detected non-stellar objects, 43 were found to be multiple observations of the same galaxies. From these repeated observations, we estimate a mean velocity error equal to $294 \pm 50 \text{ km s}^{-1}$, which is in good agreement with the value of 276 km s^{-1} obtained for the VVDS using the same VIMOS instrumental setup. The error distribution for the corresponding pairs of spectroscopic redshift is plotted in Fig. 6. In conclusion, reliable VIMOS spectra are available for 512 non-stellar objects, which span the I -band magnitude range from 19 to about 22.5, and reach $z = 0.85$ ¹⁰.

This sample was expanded by considering 101 additional objects in the field of RXCJ 0014.3-3022, selected from publicly available spectroscopic redshifts in *NED*. Cross-correlation of this new sample with our WFI photometric catalogue showed that the additional objects are mainly brighter than $R = 22.0$ (see Fig. 7). Furthermore, 24 out of the 101 objects with spectroscopic redshifts in *NED* corresponded to objects at $0.06 \leq z \leq 0.35$ observed by us. Comparison of the photometric redshifts of the corresponding pairs allowed the external error of our redshift determinations to be assessed: it is equal to $276 \pm 55 \text{ km s}^{-1}$, on average, which is fully consistent with the internal error of the same measurements.

The final catalogue of spectroscopically confirmed members of RXCJ 0014.3-3022 comprises 190 different objects, 101 of which have VIMOS spectra. In the corresponding CM diagram, the red sequence is visible (see Fig. 7); its fit, according to the same selection criteria as those used in Sect. 3.1.1, is:

$$(B - R) = (3.023 \pm 0.277) - (0.042 \pm 0.004) \times R.$$

¹⁰ Three quasars at $z = 1.02, 2.51, \text{ and } 3.08$ were also detected.

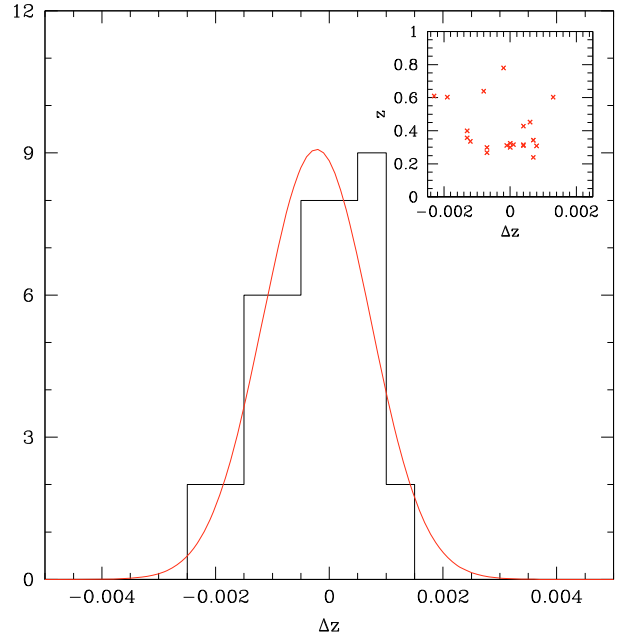


Fig. 6. Distribution of the errors on spectroscopic redshifts for multiply-observed galaxies in the region of RXCJ 0014.3-3022. In the main plot, a Gaussian fit to this distribution is also reproduced. In the upper right inset, the same errors (in abscissa) are plotted against the associated redshifts. No clear correlation is found for these galaxies, which mostly lie at the same redshift of the cluster.

The red sequence defined by spectroscopic members lying within $3'$ of the centre of RXCJ 0014.3-3022 and with $17 \leq R \leq 20$ exhibits a slightly higher normalisation and rms scatter (0.049), together with a slightly steeper slope, than the locus defined by analogous photometric cluster members. Differences are not statistically significant however.

Finally, we note that there are three very blue objects (i.e., with $(B - R) \leq 1$) even in the inner region of RXCJ 0014.3-3022, i.e., within a clustercentric distance of about 800 kpc. This is consistent with the presence of enhanced star-formation activity even there, as found by Couch et al. (1998) and BPB07, although phase-space projection effects cannot be completely excluded.

3.2.2. RXCJ 2308.3-0211: spectroscopic members

For the region encompassing RXCJ 2308.3-0211, a total of 1122 slits is available from our VIMOS spectroscopy. They provide 1522 spectra, since 424 slits contained multiple objects: 64 spectra correspond to faint stars, whereas 446 were of too poor S/N . As a result, 1012 spectra of non-stellar objects were collected, which span the redshift range $0 \leq z \leq 0.85$ ¹¹, of which 104 result to be multiple observations. This gives an intrinsic error on spectroscopic redshifts equal to $254 \pm 49 \text{ km s}^{-1}$, in good agreement with our previous determination and the VVDS one (cf. Sect. 3.2.1). In conclusion, the catalogue of VIMOS galaxy spectra in the region of RXCJ 2308.3-0211 consists of 902 robustly identified objects. No additional spectroscopic redshifts were found in *NED*.

According to the procedure of assigning cluster membership previously described, the final catalogue of spectroscopically

¹¹ Six quasars at $z = 1.09, 1.32, 2.01, 2.04, 2.14, \text{ and } 3.16$ were also detected.

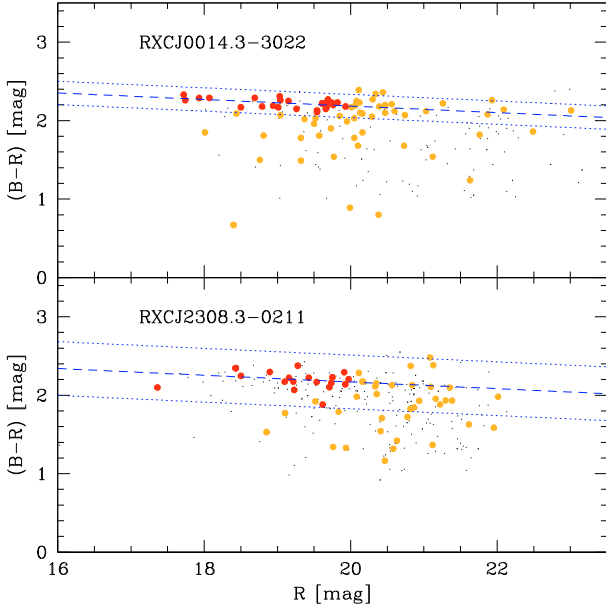


Fig. 7. The same as in Fig. 5 but for the spectroscopic members of each cluster. The red sequences defined by either spectroscopic or photometric members lying within $3'$ from the centre of each cluster are identical.

confirmed members of RXCJ 2308.3-0211 comprises 269 galaxies. The fit of the corresponding red-sequence members gives:

$$(B - R) = (3.026 \pm 0.748) - (0.043 \pm 0.013) \times R \pm 0.114.$$

Comparison of the analogous loci defined by photometric or spectroscopic members of RXCJ 2308.3-0211 confirms the behaviour found for RXCJ 0014.3-3022. The same holds for the comparison of fits obtained for the two clusters. Therefore, the fit of the photometric members of the red sequence of either cluster will be used hereafter, since this is based on higher number statistics.

No spectrum exists for the BCG of RXCJ 2308.3-0211, which sits at the cluster centre (Pierini et al. 2008). Interestingly, there is a spectroscopic member with about 60% of the R -band luminosity of the BCG (see Fig. 7). It lies at a clustercentric distance of $55''$ (i.e., about 240 kpc at the cluster’s redshift) from the cluster centre; it was not considered in the analysis made by the previous authors.

3.3. Cluster morphology: hot gas vs. galaxies

The available X-ray surface brightness distributions (Zhang et al. 2006), which indicate the dynamical state of the hot gas (Jones & Forman 1992), were complemented with surface density maps of member galaxies for the two clusters, determined as described in Appendix A. Comparison of the two-dimensional distributions of hot gas and galaxies improves our knowledge of the substructure and large-scale structure in and around the clusters.

The entire population of photometric member galaxies of a cluster and its red and blue subpopulations were considered separately. In all three cases, the same smoothing to enhance the structure against a smooth background and final spike cleaning is used, which consists of a Gaussian kernel of $100''$. Galaxy density maps were always extracted with the same resolution (mesh width of $10''$) to directly compare results. Spectroscopic catalogues were also considered, although they cover only a fraction of the region imaged by WFI. In this case, the mesh width

Table 5. Definition of regions of interest in RXCJ0014.3-3022.

Region	Radius	Angle	Objects	Area
Cluster core	$0' \leq r \leq 3'$	$0 \leq \theta \leq 360$	304	9π
NW filament	$3' < r \leq 15'$	$-10 \leq \theta \leq 50$	359	36π
S filament	$3' < r \leq 15'$	$260 \leq \theta \leq 320$	374	36π
BG field	$6' < r \leq 18'$	$120 \leq \theta \leq 210$	488	72π

Areas are expressed in square arcminutes.

and smoothing scale were increased to $20''$ and $250''$, respectively, to compensate for the poorer statistics, and, thus, to ensure convergence and avoid the occurrence of spikes produced by undersampling. Table 4 provides results from the calculation of the smooth background calculation for all catalogues used. In all cases, the rms value of the smooth background is used as a standard unit in estimating the overdensity associated with a given structure.

3.3.1. RXCJ 0014.3-3022

The complex morphology of RXCJ 0014.3-3022 on different scales was illustrated by Böhringer et al. (2006) and BPB07, with different tracers and techniques. In particular, there is evidence of two extended filamentary structures of galaxies stemming from the main body of this merging cluster, one heading to the North-West (NW), the other to the South (S). Here we use the same subregions identified in BPB07, i.e., the cluster core, the two filaments, and a neighbouring, low-density region assumed to represent the coeval “field” environment unaffected by the cluster. The statistics of the field was used to determine significant overdensities. The geometrical criteria (in addition to those considering observed magnitude and photo- z) behind the definition of each subregion (and corresponding subcatalogue) are listed in Table 5. There the criteria are expressed as local polar coordinates with respect to the cluster centre, where the clustercentric distance is expressed in arcminutes, the polar angle in degrees (with the zero angle towards E and increasing counter-clockwise w.r.t. the observer) and the enclosed area in square arcminutes.

The main body of RXCJ 0014.3-3022 is elongated in the NW-SE direction, which is where the two main clumps of galaxies are located, but it also exhibits plenty of scattered extensions. The most outstanding ones are the two filaments to the NW and S, which can be traced out to about $9'$ (i.e., 2.44 Mpc) and certainly extend beyond the imaged region of the cluster, and, thus, beyond the X-ray R_{200} (2.52 Mpc, Zhang et al. 2006). These two elongated structures host about the same number of galaxies, and as many as the core, which however occupies an area four times smaller. The S filament is more clearly evident as a twisted chain of high-density lumps, whereas the NW filament appears as a smoother distribution of slightly overdense peaks (see Fig. 8). Unsurprisingly, red galaxies mainly represent the main body of the cluster, but they also trace the inner part of the filaments. In addition to the two central clumps each associated with BGC pairs (see Pierini et al. 2008), a third, less dense clump of red galaxies lies slightly to the N w.r.t. the cluster centre: it hosts a fifth BCG, as anticipated (see Sect. 3.2.2). An additional overdensity of red galaxies (w.r.t. to the field) lies to the SE; it appears as detached from the main body of the cluster.

The overall picture is confirmed by the distribution of the spectroscopically confirmed cluster members. Although the available spectroscopy does not extend to the outer edges of the filaments, at least the inner part of the S filament is traced by

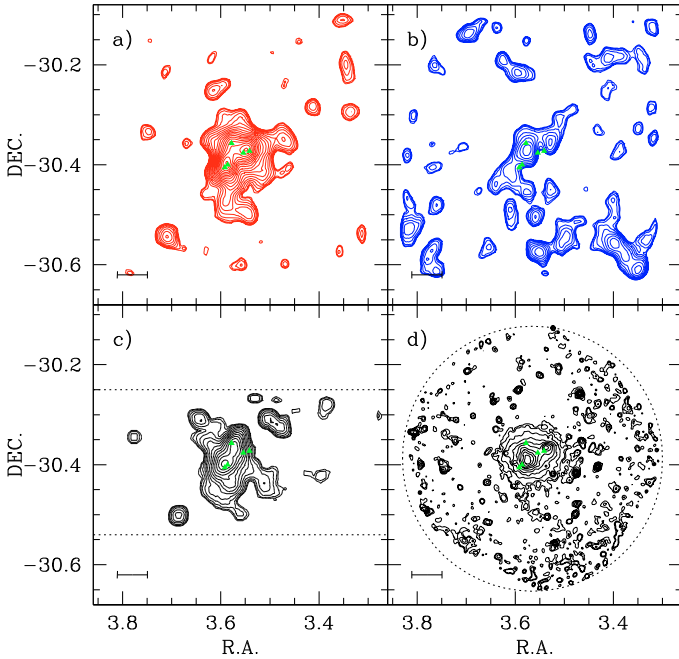


Fig. 8. Galaxy density maps and X-ray image for RXCJ0014.3-3022. Panels **a)** and **b)** show, respectively, the density maps of red and blue photometric members. Panel **c)** shows the density map of spectroscopic members instead, where dotted lines mark the approximate extent of the VIMOS combined pointings. Panel **d)** shows the distribution of the X-ray emitting, hot gas, where a dotted circle marks the approximate FOV of XMM-Newton. Green triangles mark the positions of the BCGs of every galaxy clumps. In all maps, reproduced contours have a significance of at least 5σ w.r.t. the background. The lower left horizontal bar has a size of 1 Mpc at the cluster’s redshift.

spectroscopic cluster members. Remarkably, the same conclusion can be reached from the X-ray surface brightness distribution (Fig. 8) and entropy map (Böhringer et al. 2006) of the hot gas. Unsurprisingly, filaments are more closely traced by blue galaxies. Nevertheless, an overdensity of blue galaxies (w.r.t. the field) lies exactly between the three clumps of red galaxies associated with BCGs previously described. Its presence is consistent with the findings of Couch et al. (1998). In addition, two regions with a less marked overdensity of blue galaxies are discovered, which extend the two main clumps of red galaxies in the main body of the cluster. One of them is led by an X-ray bowshock detected by *Chandra* (see Kempner & David 2004) and associated with the NW subcomponent of this merging cluster. As discussed in BPB07, this shock may shield infalling galaxies from the surrounding ICM, which enables them to continue their normal star-formation activity.

3.3.2. RXCJ 2308.3-0211

In X-rays, RXCJ 2308.3-0211 appears as an azimuthally symmetric, centrally concentrated system, as is typical of cool-core clusters. For the region of this cluster, we define five subregions (see Table 6): the cluster core, two outer, concentric circular annuli, and two low-density regions (i.e., “fields”). We note that the total circular area occupied by the cluster, defined as the sum of the core and the two annular regions, contains 980 galaxies within a radius of $9'$. For comparison, RXCJ 0014.3-3022 hosts 1016 galaxies within the same clustercentric distance. Furthermore, the total area of the field regions for

Table 6. Definition of regions of interest in RXCJ2308.3-0211.

Region	Radius	Angle	Objects	Area
Cluster core	$0' < r \leq 3'$	$0 \leq \theta \leq 360$	258	9π
Inner outskirts	$3' < r \leq 6'$	$0 \leq \theta \leq 360$	293	27π
Outer outskirts	$6' < r \leq 9'$	$0 \leq \theta \leq 360$	429	45π
BG field (1)	$9' < r \leq 19'$	$200 \leq \theta \leq 240$	255	31.1π
BG field (2)	$9' < r \leq 19'$	$300 \leq \theta \leq 350$	228	38.9π

Areas are expressed in square arcminutes.

RXCJ 2308.3-0211 is equivalent to the area of the field for RXCJ 0014.3-3022; it also contains the same number of objects.

Consistently with the cool-core nature of the cluster, the distribution of red galaxies is centrally concentrated, the BCG itself residing at the cluster centre. However, the optical morphology of the cluster is less regular, as confirmed by the two-dimensional distribution of spectroscopic cluster members. Furthermore, two pronounced overdensities of red galaxies lie to the N of RXCJ 2308.3-0211, about $15'$ (i.e., ~ 4.1 Mpc) away from it. They are well beyond the X-ray R_{200} of the cluster (2.44 Mpc; Zhang et al. 2006) and are separated by $\sim 4'$ (i.e., about 1.2 Mpc). These two structures are probably groups that are not detected in X-rays as well, although they lie at the edge of the XMM-Newton image. Both the red galaxy density distribution and the two-dimensional distribution of spectroscopic cluster members suggest the existence of a bridge between these two groups and RXCJ 2308.3-0211. This also compares well with the weak-lensing analysis in Dahle et al. (1980), where the mass distribution is seen to be elongated towards N. An additional overdensity of spectroscopic members eastwards of the main cluster coincides with similar structures in the red galaxy map and the X-ray image. A Dressler-Schechtman analysis (Dressler & Schechtman 1988) suggests that this structure is likely a group that is still not connected to the cluster (Braglia et al. 2009b, in prep.). Finally, there are extremely few overdense structures traced by blue galaxies, across the WFI image: the main ones form a sequence of blobs jutting out of the cluster centre in the NE direction.

3.4. Spectral indices: global behaviour of galaxy populations

The strength of the 4000 \AA break ($D4000$) and the equivalent widths of the H_δ photospheric absorption line and the [OII] nebular emission line ($W_0(H_\delta)$ and $W_0(\text{[OII]})$), respectively) could be robustly determined from VIMOS spectra with $S/N > 4$ for galaxies at $z \sim 0.3$. An analysis based on these spectral features can constrain the star-formation histories of individual cluster members (e.g., Balogh et al. 1999; throughout this paper, we use the same definition as adopted there, where $W_0(\text{[OII]})$ is positive when in emission and $W_0(H_\delta)$ is positive in absorption). The spectral index $D4000$ is particularly sensitive to the presence of old (i.e., $\geq 1-2$ Gyr), passively evolving stellar populations. In contrast, $W_0(H_\delta)$ is sensitive to episodes of star-formation in the past Gyr, since it measures the presence of A-type stars, whereas $W_0(\text{[OII]})$ estimates the present star-formation activity (i.e., the SFR on timescales of ≤ 0.01 Gyr). The combined use of the diagnostic diagrams $W_0(H_\delta) - W_0(\text{[OII]})$ and $W_0(H_\delta) - D4000$ helps to prevent misinterpretations due to non introducing corrections for intrinsic dust extinction or additional line emission affecting $W_0(\text{[OII]})$ and $W_0(H_\delta)$, respectively.

The behaviour of each spectral index as a function of the observed $(B - R)$ colour (uncorrected for internal extinction)

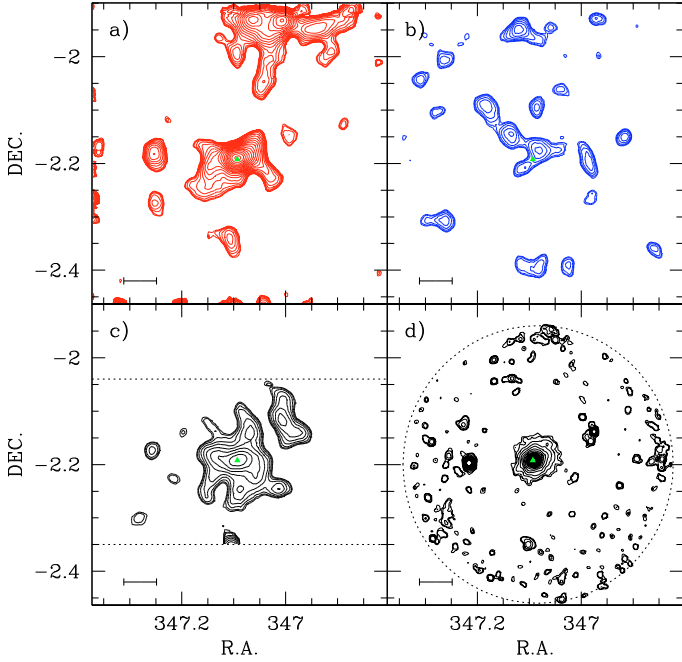


Fig. 9. The same as in Fig. 8 but for RXCJ 2308.3-0211.

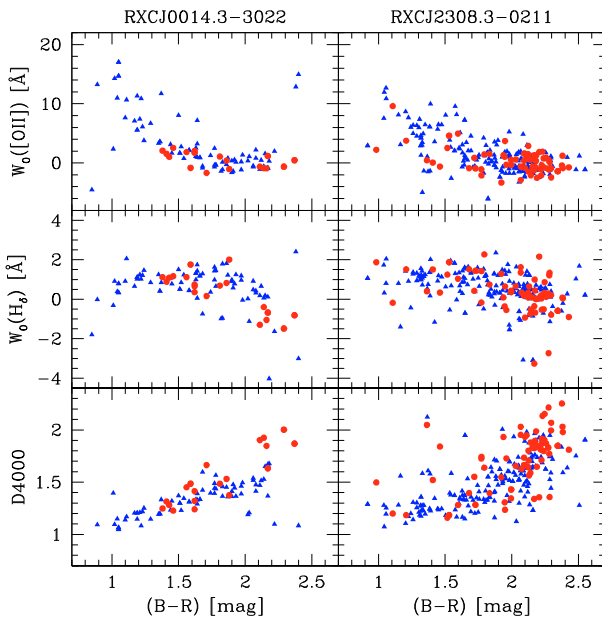


Fig. 10. Spectral indices $W_0(H_\delta)$, $W_0([OII])$, and D4000 (see text) as a function of $(B-R)$ colour (observed frame) for spectroscopic members of RXCJ 0014.3-3022 (left column) and of RXCJ 2308.3-0211 (right column). Triangles and circles mark sub- L^* (i.e., with $L_R < L_R^*$) and luminous galaxies, respectively.

for the spectroscopic members of each cluster is reproduced in Fig. 10. Unsurprisingly, galaxies with redder $(B-R)$ colours tend to exhibit lower values of $W_0([OII])$ (i.e., less emission in the $[OII]$ line) and higher values of D4000. Hence, they have experienced a lower star-formation activity in the past Gyr or so, and, thus, tend to be dominated by old, passively evolving stellar populations. Interestingly, this is true irrespective of the galaxy luminosities.

In analogy with previous spectral index analyses (e.g., Barger et al. 1996; Balogh et al. 1999), we determine empirically threshold values for the three spectral indices to discriminate

Table 7. Definitions in the $[W_0([OII]), W_0(H_\delta)]$ plane.

Definition	$W_0([OII])$	$W_0(H_\delta)$
PEV (passive)	< 4.85	≤ 5
SF (star-forming)	≥ 4.85	$\in [0, 5]$
SSB (short starburst)	≥ 4.85	< 0

Table 8. Definitions in the $[D4000, W_0(H_\delta)]$ plane.

Definition	D4000	$W_0(H_\delta)$
PEV (passive)	≥ 1.4	≤ 5
SF (star-forming)	< 1.4	$\in [0, 5]$
SSB (short starburst)	< 1.4	< 0

different star-formation regimes. In particular, red sequence galaxies identified photometrically (cf. Sects. 3.1 and 3.2) are used to determine the mean and rms of $W_0([OII])$, $W_0(H_\delta)$, and D4000 that are assumed to represent galaxies dominated by old, passively evolving stellar populations. These are defined as the objects with indices within 3σ of the mean of $W_0([OII])$ or D4000, which operationally translates into: $W_0([OII]) < 4.85 \text{ \AA}$ in the $W_0([OII])$ – $W_0(H_\delta)$ diagnostic diagram, or $D4000 \geq 1.4$ in the $D4000$ – $W_0(H_\delta)$ one. These thresholds are consistent with those adopted by Balogh et al. (1999) or Dressler et al. (1999), according to their samples and data (i.e., $W_0([OII]) = 5 \text{ \AA}$ and $D4000 = 1.45$, respectively). Following these authors, we adopt $W_0(H_\delta) = 0 \text{ \AA}$ as a threshold between normal star-forming and (short) starburst galaxies.

In the absence of detected objects with extreme values of $W_0(H_\delta)$ in our samples, the spectroscopically confirmed member galaxies of our clusters belong to one of the following three classes (see also Tables 7 and 8; cf. Balogh et al. (1999)):

Passive galaxies (PEV): systems currently not undergoing traceable star-formation activity, mainly with E or S0 spectral type (and morphology). They are defined by $W_0(H_\delta) \leq 5 \text{ \AA}$ and $W_0([OII]) < 4.85 \text{ \AA}$, or $D4000 \geq 1.4$.

Star-forming galaxies (SF): systems that have been undergoing significant star-formation activity for at least several hundred million years, mainly identified as late-type galaxies (spirals and irregulars). They are identified by $0 \leq W_0(H_\delta) \leq 5 \text{ \AA}$ and $W_0([OII]) \geq 4.85 \text{ \AA}$, or alternatively $D4000 < 1.4$.

Short-starburst galaxies (SSB): systems currently undergoing a short-lived, intense episode of star-formation (i.e., ≤ 200 Myr), where nebular emission is strong. They have $W_0(H_\delta) < 0 \text{ \AA}$ and $W_0([OII]) \geq 4.85 \text{ \AA}$, or alternatively $D4000 < 1.4$.

Although none of the cluster members fall into the following definition, we introduce an additional class useful in our analysis, the so-called *post-starburst galaxies* (Dressler & Gunn 1983; Poggianti et al. 1999). These systems show negligible emission lines but strong Balmer absorption; this suggests that star-formation activity in these systems ended abruptly in the recent past. According to Poggianti et al. (1999) and our previous definitions, we define these systems as having $W_0(H_\delta) \geq 5 \text{ \AA}$ and $W_0([OII]) < 4.85 \text{ \AA}$.

The diagnostic diagrams $W_0([OII])$ – $W_0(H_\delta)$ and $D4000$ – $W_0(H_\delta)$ establish that RXCJ 0014.3-3022 and RXCJ 2308.3-0211 host overall different galaxy populations (see Fig. 11). A diagnostic two-dimensional Kolmogorov-Smirnov test (Fasano & Franceschini 1987; Peacock 1983), executed for the distribution of members of either cluster in the two previous diagnostic diagrams, concludes that the probability that the two

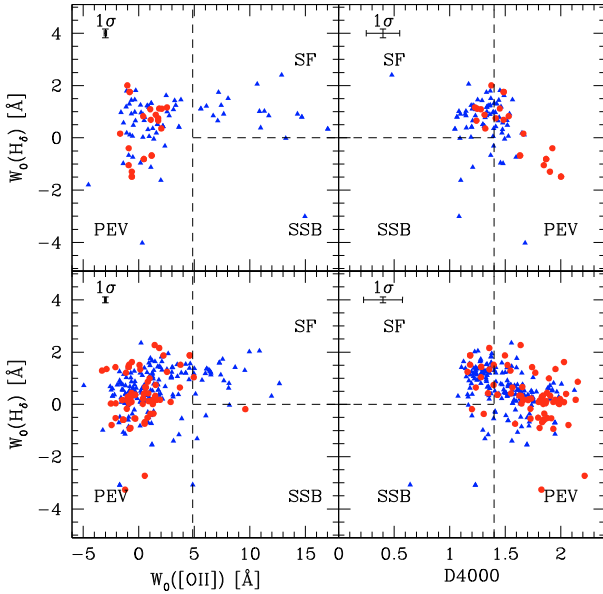


Fig. 11. Spectral index diagnostic diagrams for spectroscopic members of RXCJ0014.3-3022 (top row) and of RXCJ2308.3-0211 (bottom row). In each panel, 1σ uncertainties are shown, whereas dashed lines mark thresholds for discriminating different star-formation regimes (see Tables 7 and 8). Symbols are the same as in Fig. 10.

distributions are drawn from the same parent population is absolutely negligible: 0.02% for the $D4000-W_0(H\delta)$ plane, and 0.41% for the $W_0([OII])-W_0(H\delta)$ plane. The significant difference between the galaxy populations of the two clusters is not due to selection effects, since the selection function of spectroscopic targets was the same (cf. Sect. 2.2).

This is confirmed by the different distribution of spectroscopic cluster members in the $D4000-(FUV - V)$ colour (rest frame¹²) plane (cf. Moran et al. 2007), as shown in Fig. 12. These galaxies are flagged as passive or star-forming according to their values of $W_0([OII])$. Out of 101 (269) spectroscopic members of RXCJ0014.3-3022 (RXCJ2308.3-0211), 12 (7) were detected by GALEX in the FUV¹³. It is evident that not only the fraction of FUV-detected member galaxies, but also the overall distribution of member galaxies with lower limits to $(FUV - V)$ is different. In particular, the bulk of spectroscopic members of RXCJ2308.3-0211 does not exhibit $(FUV - V) < 2$ (rest frame), regardless of the value of $D4000$, whereas RXCJ0014.3-3022 hosts a non-negligible population of galaxies with $D4000 < 1.6$ and $(FUV - V) < 2$. We attribute the strong differences in galaxy populations between RXCJ0014.3-3022 and RXCJ2308.3-0211 to the largely different dynamical states and morphologies of the two clusters (see Sect. 3.3 and Braglia et al. 2009b, in prep.).

Finally, we note that both clusters host a small but odd population of galaxies with $(B - R) \geq 2$ and either $D4000 < 1.4$ or $W_0([OII]) \geq 4.85 \text{ \AA}$. In RXCJ0014.3-3022 these few objects are sub- L^* , whereas there are some luminous ones in RXCJ2308.3-0211. We tentatively interpret this odd class of red galaxies with evidence of recent or present star-formation activity as dusty galaxies with very different SFRs (cf. Verdugo et al. 2008). They

¹² GALEX FUV and WFI V -band magnitudes of individual objects are k -corrected according to the best-fit templates in *HyperZ*.

¹³ Most of the FUV-detected galaxies in RXCJ0014.3-3022 lie close to the cluster core and in the region of the S filament, in correspondence of the clumps of blue galaxies discussed in Sect. 3.3.

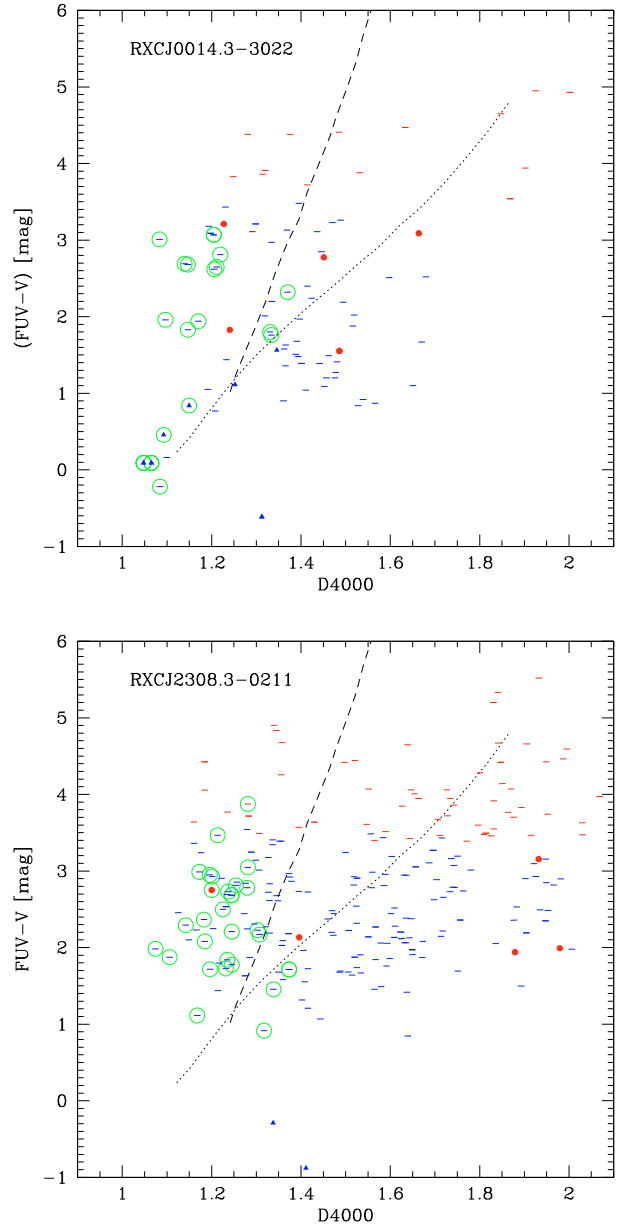


Fig. 12. Rest-frame $(FUV - V)$ colour as a function of $D4000$ for the spectroscopic members of RXCJ0014.3-3022 (top) and of RXCJ2308.3-0211 (bottom). In each panel, symbols are the same as in Fig. 10. In addition, red and blue bars mark lower limits on $(FUV - V)$ for luminous and sub- L^* galaxies, respectively. Furthermore, green circles mark galaxies with significant $[OII]$ emission (i.e., $W_0([OII]) \geq 4.85 \text{ \AA}$). Finally, dashed and dotted lines mark, respectively, models corresponding to a starvation or a truncation evolutionary track, similarly to Moran et al. (2007).

are however not post-starburst galaxies, since they do not show a large absorption in the $(H\delta)$ line (i.e. ≥ 5). There is now substantial observational evidence from IR observations that cluster galaxies can experience strongly obscured star-formation activity (e.g., Metcalfe et al. 2005; Saintonge et al. 2008, and references therein). This population of dust-obscured star-forming galaxies seems particularly abundant in galaxy clusters undergoing merging and strong episodes of mass accretion (e.g., Coia et al. 1999; Tran et al. 2005; Loh et al. 2008), with little dependence on the mass of the parent system as they are also observed in groups (Wilman et al. 2008). A large fraction of these dusty

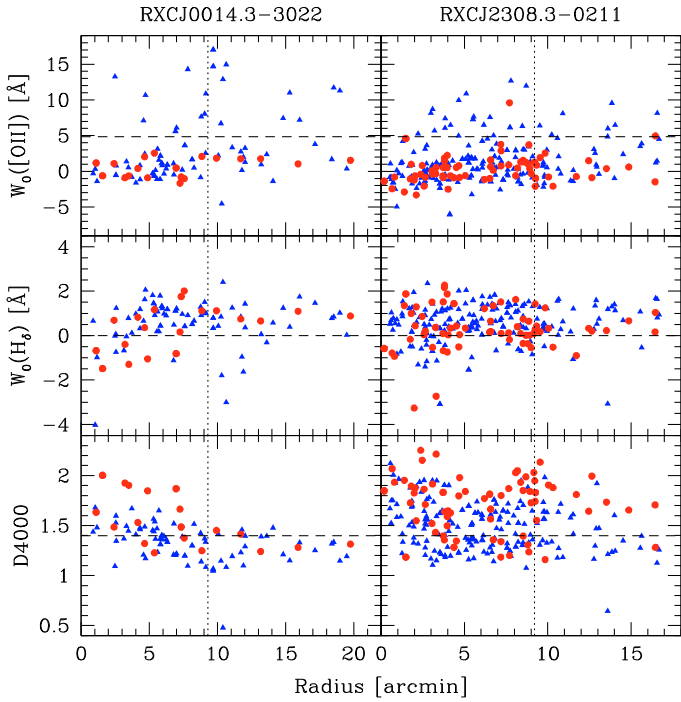


Fig. 13. Behaviour of spectral indices as a function of cluster-centric distance for spectroscopic members of RXCJ0014.3-3022 (left column) and of RXCJ2308.3-0211 (right column). Symbols are the same as in Fig. 10. In each panel, the horizontal dashed line marks the characteristic threshold for the given index, whereas the vertical dotted line marks the distance corresponding to R_{200} .

galaxies are classified as early-type spirals (e.g., Biviano et al. 2004; Wilman et al. 2008), in agreement with the average spectral type of our red, star-forming population.

3.5. Spectral indices: local behaviour of galaxy populations

Here we investigate whether differences in galaxy populations between RXCJ0014.3-3022 and RXCJ2308.3-0211 arise in well defined regions of the two clusters. Firstly, we analyse the behaviour of the spectral indices of spectroscopically confirmed members as a function of the clustercentric distance (see Fig. 13). In RXCJ0014.3-3022, spectroscopic members tend to exhibit $D4000 < 1.4$ when their clustercentric distances approach or exceed the value of R_{200} . The increase in the fraction of star-forming systems towards and beyond R_{200} is confirmed by the corresponding behaviours of $W_0([OII])$ and $W_0(H_\delta)$. This is consistent with the existence of a sharp peak in the fraction of blue-to-red galaxies along the two filaments (see BPB07) especially the southern one, which is poorly sampled by the available VIMOS data (see Fig. 1). Conversely, the combined behaviour of the same spectral indices for spectroscopic members of RXCJ2308.3-0211 as a function of clustercentric distance shows that passive galaxies dominate everywhere in this cluster. Furthermore, luminous galaxies (i.e., with $L_R \geq L_R^*$) tend to be passive already beyond R_{200} in RXCJ2308.3-0211, whereas passive, luminous galaxies almost exclusively populate regions within R_{200} in RXCJ0014.3-3022. Analogous differences exist when considering the population of sub- L^* galaxies in the two clusters. This suggests that galaxies already tend to be passive and, thus, populate the red sequence outside the virialized region in RXCJ2308-0211, in agreement with previous findings for other clusters (Kodama et al. 2001, 2003; Balogh et al. 1997).

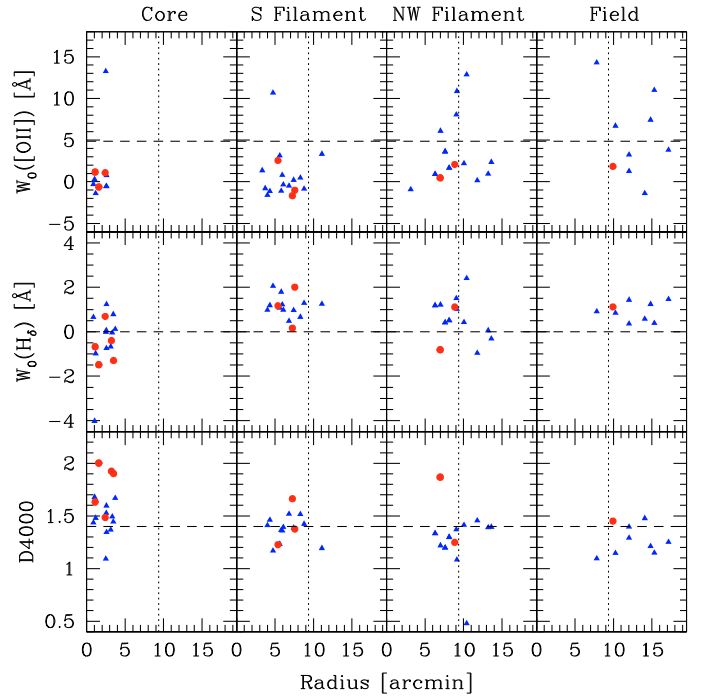


Fig. 14. Behaviour of spectral indices as a function of cluster-centric distance for different regions of RXCJ0014.3-3022 (see Table 5). Symbols and lines are the same as in Fig. 13.

In particular, Balogh et al. (1997) found that star-formation in cluster galaxies is generally suppressed (w.r.t. the field) out to $2R_{200}$. In contrast, galaxies tend to populate the red sequence mostly inside the virialized region in RXCJ0014.3-3022.

To understand these differences more clearly, we investigate subregions of the two clusters as well as their neighbouring fields. As for RXCJ0014.3-3022 (Fig. 14), spectroscopic members in the core region are mostly passive at variance with the galaxy population in the neighbouring field. This contains a mixture of passive and mildly-to-highly star-forming systems. Nevertheless, there is additional evidence of (mostly faint) galaxies with intense star-formation activity in the cluster core (see Couch et al. 1998). Spectroscopic members associated with the two filaments of RXCJ0014.3-3022 exhibit properties in between those of the galaxy populations in the cluster core and the neighbouring field. Unfortunately, the present VIMOS data do not extend much beyond R_{200} in the direction of the S filament, where most of the “flaming giants” discovered by BPB07 lie.

As for RXCJ2308.3-0211, the star-formation activity of spectroscopic members appears to be low everywhere, but tends to increase towards R_{200} (cf. Fig. 13, right panel). Consistently, $D4000$ tends to decrease from the core to the outskirts of the cluster. Star-formation activity appears to be almost exclusively present in sub- L^* galaxies. This picture agrees with previous results in the literature (e.g. Balogh et al. 1999). However, the paucity of star-forming galaxies, not only among the luminous ones, is evident also in the neighbouring field.

4. Discussion

RXCJ0014.3-3022 and RXCJ2308.3-0211 are two clusters at $z \sim 0.3$ with comparable X-ray luminosities¹⁴ (and thus, likely, total masses), but with opposite X-ray morphologies

¹⁴ Respectively 1.29 and 1.02×10^{45} erg s⁻¹.

(i.e., dynamical states): the former is a merging system, the latter a regular, centrally concentrated one. The optical morphologies of both clusters are more complex than their X-ray ones. In addition to the two X-ray subcomponents, RXCJ 0014.3-3022 exhibits two extended filaments (one of which is tentatively detected in X-rays) and a core rich in substructure, as traced by galaxies with photometric or spectroscopic redshifts consistent with that of the cluster. Furthermore, its core hosts two visual pairs of BCGs, each associated with a displaced X-ray subcomponent (see Pierini et al. 2008, for a discussion), and an additional equally luminous BCG located in a third overdense region. On the other hand, the X-ray centroid of RXCJ 2308.3-0211 coincides with the position of its BCG, as expected for a cool-core cluster, but photometric or spectroscopic cluster members define a core region that is less centrally symmetric than in X-rays. The difference between the optical and X-ray shapes can be explained well in terms of the different properties of the various cluster components. The gas particles have isotropic motions, and thus follow isopotential contours that are smoother than the distribution of galaxies and dark matter, which instead show non-isotropic velocity distributions. Moreover, the X-ray surface brightness follows the projected square density of the gas and thus emphasises the more regular central region, mainly missing the irregular outskirts where the gas density is low.

In spite of the evident difference in assembly state at $z \sim 0.3$, these clusters exhibit the same locus of galaxies dominated by old, passively-evolving stellar populations¹⁵. The red sequence of each cluster is well populated, both by photometric or spectroscopic members.

However, the star-formation history of the average galaxy is quite different for the two clusters, as confirmed by spectral index analysis of their spectroscopic members. Combining information from the distributions of these galaxies in the $W_0(\text{[OII]})-W_0(\text{H}_\delta)$, $\text{D4000}-W_0(\text{H}_\delta)$, and $\text{D4000}-(\text{FUV} - V)$ planes¹⁶ offers the consistent picture that star-formation activity is rapidly moving towards a quiescent state, if it is not already absent, across the virialized region of RXCJ 2308.3-0211, whatever the R -band luminosity of its spectroscopic members. This is confirmed by comparison of the distributions in the $\text{D4000}-(\text{FUV} - V)$ plane of real galaxies and models corresponding to evolutionary scenarios for either starvation or (abrupt) truncation of the star-formation activity (Moran et al. 2007). In both clusters, we recover the standard scenario that the overall stellar population in galaxies tends to become younger towards the outskirts (e.g., Balogh et al. 1999). In RXCJ 2308.3-0211, this is mostly due to (residual) star-formation activity in sub- L^* galaxies, since even the neighbouring field contains galaxies with $L_R \geq L_R^*$ as red as luminous red-sequence galaxies in the cluster core.

In contrast, RXCJ 0014.3-3022 contains a sizeable fraction of actively star-forming systems even within R_{200} and beyond. This happens in different subregions of this merging cluster for different reasons. Sub- L^* starburst systems in the cluster core were discovered by Couch et al. (1998); which were found to experience strong tidal interactions. Both sub- L^* and luminous star-forming systems populate the two filaments stemming out of the cluster main body and reaching R_{200} and beyond (BPB07). The former can be interpreted as infalling low-mass systems that manage to keep part of their still conspicuous HI gas

reservoir, consistently with the generally accepted “downsizing” scenario (Lilly et al. 1996; Gavazzi & Scodreggio 1996; Gavazzi et al. 1996; Cowie et al. 1999), in spite of the growing influence of the cluster environment. The latter were interpreted by BPB07 as relatively high-mass galaxies with residual HI gas in their discs experiencing “harassment” (cf. Moore et al. 1996, 1998, 1999). After an average increase in star-formation activity across R_{200} (BPB07), star-forming galaxies of all masses along the filaments appear to move towards the red sequence as their clustercentric distances become smaller and smaller with respect to R_{200} . This is consistent both with the starvation scenario (Balogh et al. 1999) and with galaxy harassment, as well as with the later removal of residual HI gas by ram pressure stripping by the ICM (e.g., Gunn & Gott 1972; Quilis et al. 2000; Tonnesen & Bryan 2008) in the cluster core.

In conclusion, RXCJ 2308.3-0211 appears to be a massive system that is already assembled at $z \sim 0.3$, and sits in a large-scale environment where most galaxies are dominated by old, passively-evolving stellar populations (cf. the two groups well beyond the cluster virial radius). In contrast, the massive, merging system RXCJ 0014.3-3022 sits in a large-scale environment where galaxies of different masses can still form stars, as occurs in its core and filaments. Nevertheless, galaxies dominated by old, passively-evolving stellar populations are the most frequent ones in its core, and define the same locus as those in the core of RXCJ 2308.3-0211, although with half the scatter. This is consistent with the previous picture that a larger and more heterogeneous fraction of the overall galaxy population stopped forming stars a long time ago or is rapidly moving towards a quiescent star-formation activity in RXCJ 2308.3-0211, whereas in RXCJ 0014.3-3022 only the massive galaxies populating the cluster core have done so.

This is also reflected in the different scatter observed for the two clusters’ red sequences. The tighter red sequence observed in RXCJ 0014.3-3022 can be ascribed to this cluster only having its pristine red sequence, i.e., its primordial population of old, evolved galaxies, the large fraction of observed active objects having not yet moved to the red sequence. Conversely, RXCJ 2308.3-0211 has much fewer star-forming systems, hence the largest part of the galaxies has already moved to the red sequence. If, consistently with the already described picture, at least part of these galaxies have just recently moved to the red sequence, then these younger additions will increase the observed scatter before finally settling onto the main red sequence.

Our results support an inside-out scenario for the build-up of the red sequence (e.g., Lidman et al. 2008). They also suggest the existence of a link between assembly history and average star-formation activity in member galaxies of clusters with similar masses in general. This could explain the large variation in the evolutionary phases of galaxies in groups with similar masses at redshifts lower than $z \sim 1$ (Tanaka et al. 2008). Studies based on larger data sets and multiwavelength information than in the present paper are necessary to elucidate this matter.

5. Conclusions

The link between the dynamical state and star-formation history of member galaxies has been investigated for two X-ray luminous clusters at $z \sim 0.3$, i.e., the merging system RXCJ 0014.3-3022 and the cool-core system RXCJ 2308.3-0211. The richness of spectroscopic information and the quality of photometric data allow differences in galaxy populations to be traced not only as a function of clustercentric distance (as done in most previous studies of clusters at similar redshifts), but also of cluster

¹⁵ This is likely even though no correction for dust attenuation is applied to the photometry of star-forming galaxies.

¹⁶ This minimises the impact of dimming and reddening effects produced by dust in star-forming galaxies.

substructure. This is more evident in maps of galaxy overdensity (w.r.t. a coeval, neighbouring “field”) based on the (observed frame) optical colour ($B - R$) and photometric redshifts.

The (observed frame) $(B - R) - R$ colour–magnitude diagrams of the inner regions of both clusters exhibit the same, well-defined locus of galaxies dominated by old, passively-evolving stellar populations (the so-called red sequence). This locus is more populated, and with a larger scatter around it, in the regular cluster RXCJ 2308.3-0211.

A combined analysis based on spectroscopic indices (i.e., the equivalent widths of the [O II] and H_δ lines and the amplitude of the 4000 Å break D4000) and (rest frame) FUV – V colours establishes the existence of substantial differences between the two clusters. In agreement with analogous studies in the literature, the capability of forming stars is found to increase with larger clustercentric distance of a member galaxy. There is also evidence of obscured star-formation activity in a small fraction of member galaxies. However, in RXCJ 2308.3-0211, the bulk of the luminous (i.e., with $L_R \geq L_R^*$) galaxy population has stopped forming stars since long, or is evolving towards a quiescent star-formation activity: it is mostly the sub- L^* galaxies that continue to form stars at substantial rates. In contrast, RXCJ 0014.3-3022 hosts luminous galaxies with enhanced star-formation activity (w.r.t. the “field”) along two filamentary structures extending from its main body and reaching its R_{200} . Furthermore, an increased fraction of (mostly sub- L^*) star-forming galaxies is found along the two filaments across R_{200} . Both phenomena are probably due to “galaxy harassment”. Finally, it was already known that sub- L^* starburst galaxies populate the core of RXCJ 0014.3-3022: they are tidally disturbed systems.

Differences in galaxy populations extend from the virialized regions to the large-scale environments of the two clusters. RXCJ 2308.3-0211 resides in a region of the universe where passive evolution of stellar populations or quiescent star-formation activity characterises at least luminous galaxies, as demonstrated by our results for the field and two groups at the same (photometric) redshift. Conversely, the two extended filaments of RXCJ 0014.3-3022 are nested inside a still “active” environment. This suggests the existence of a link between assembly history and average star-formation activity in member galaxies for (at least) X-ray selected, massive clusters at $z \sim 0.3$.

Acknowledgements. Based on observations made with ESO VLT at the Paranal Observatory under programme ID 169.A-0595. Based on observations made with the ESO/MPG 2.2 m telescope at the La Silla Observatory inside the Max Planck Gesellschaft (MPG) time. This research has made use of the NASA/IPAC Extragalactic Database (NED) which is operated by the Jet Propulsion Laboratory, California Institute of Technology, under contract with the National Aeronautics and Space Administration. F.B. acknowledges support by the International Max-Planck Research School (IMPRS) on Astrophysics. D.P. acknowledges support by the German *Deutsches Zentrum für Luft- und Raumfahrt*, DLR project number 50 OR 0405. H.B. acknowledges support by *The Cluster of Excellence “Origin and Structure of the Universe”*, funded by the Excellence Initiative of the Federal Government of Germany, EXC project number 153.

Appendix A: Density map calculation

Starting from the main catalogue of cluster photo-z members and the two sub-catalogues of red and blue objects, a fixed-width mesh is applied to the full catalogue. The mesh width is found to affect in part the final density map, mainly by smoothing small-scale density peaks; its optimal value is found to be between 7 and 10 arcsec, corresponding to a physical scale of 30 to 45 kpc at the cluster’s redshift. To ensure a robust yet fine sampling of

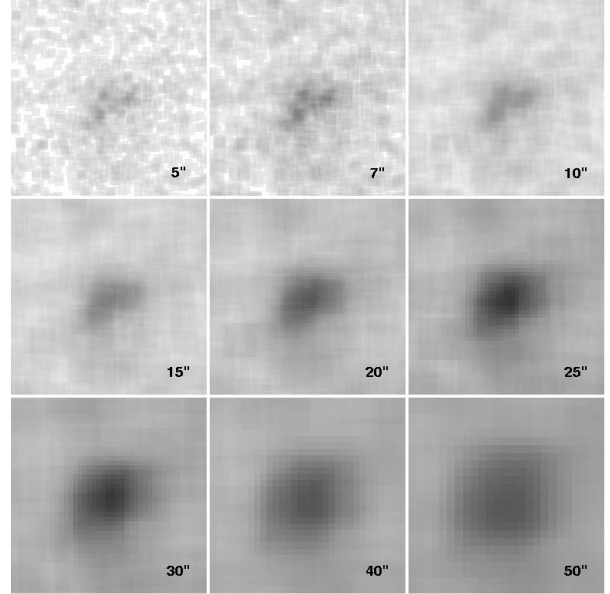


Fig. A.1. Example of density map for the central part of A2744. From top left to bottom right, density maps for different mesh widths are shown. The mesh width value in arcseconds is also shown for each map.

the cluster population, a scale of 10 arcsec was chosen. This is a small enough scale to detect and suitably map substructures in dense regions (such as the cluster core where three main prominent blobs are seen in the galaxy distribution), while ensuring a good and stable sampling of low-density regions without being heavily affected by small-scale background fluctuations. A fixed mesh width is found to map both high-density peaks and background more accurately, while adaptive meshes proved to be too sensitive to small-scale fluctuations, with the risk of a wrong evaluation of background.

Background is calculated at each mesh point by counting all objects within a fixed radius around the point. The chosen radius partly acts as a smoothing filter: this ensures a good sampling of the large-scale shape of background (to be able to evaluate correctly the background mean and rms). The background mean value and rms are then calculated by fitting the background values distribution with a Gaussian, assuming that the field should represent a population of randomly scattered objects with normal fluctuations. The Gaussian is fitted by recursive 3-sigma clipping until convergence, which is always reached with 3 to 10 cycles. The final Gaussian parameters are taken to represent the mean and rms of background.

To select the most efficient smoothing radius, several tests were completed on the sample with different radius values. The background was thus calculated with increasing radii and then fitted with a Gaussian, assuming it is dominated by random noise (i.e. randomly scattered field galaxies). The background mean value and rms are weakly sensitive to the smoothing radius for radius values between 60'' and 120''. Below 60'', small-scale fluctuations make the background dominated by small numbers, while beyond 120'' the mean slowly but steadily declines, due to the undersampling of background counts at the field borders. Between 60'' and 120'' the background value is almost stable, with errors becoming slightly lower with increasing smoothing radius. The behaviour, along with the background rms, is shown in Fig. A.3. A final smoothing scale of 110'' was chosen; this is equivalent to 500 kpc at the cluster redshift.

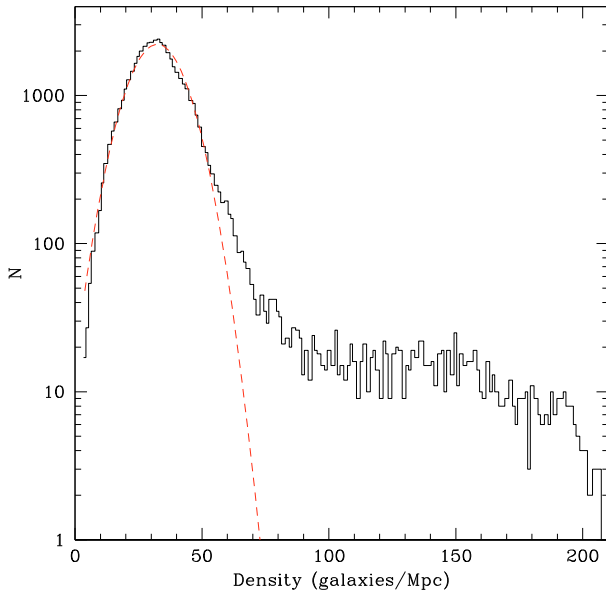


Fig. A.2. Background fit for a smoothing radius of $110''$ in the field of RXCJ 0014.3-3022. The histogram is the count distribution in the field, with the high density tail due to overdense structures (i.e. the cluster and its filaments); the dashed line is the Gaussian fit to the background.

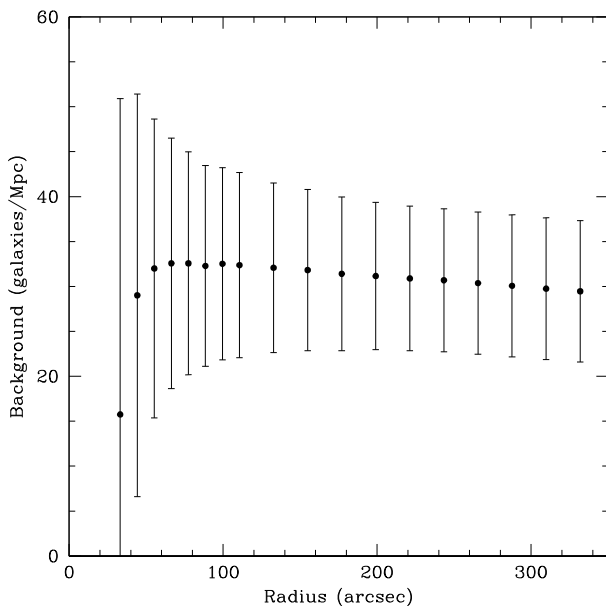


Fig. A.3. Background mean and error versus smoothing radius for the full catalogue of cluster members. For very low values (under $60''$) the value rapidly goes down due to oversampling of small fluctuations, while beyond $120''$ a trend towards lower values is due to undersampling of counts at the field border. Between $60''$ and $120''$, the background value is stable. Error bars are 1σ errors.

After evaluating background mean and rms, the true density maps are generated. First, galaxies are counted in each mesh box and their number is divided by the box area and then normalised to Mpc scale. The map is then smoothed with a Gaussian filter to clean numerical spikes (arising at the map border due to incorrect sampling) and for more continuous connection of counts in neighboring mesh cells. The same smoothing radius as for background calculation provides reliable results, cleaning spikes without deleting substructuring information. A number of simulated background maps is then generated as randomly distributed

values with normal distribution (as given by the background best-fit parameters and chosen smoothing scale); the background map is then independently subtracted from the raw density map and the resulting background-subtracted maps are stacked together and normalised. This ensures that the background subtraction remains as smooth as possible and unaffected by true overdensities in the cluster field. One hundred iterations provide a good mean background subtraction.

The background-subtracted, stacked and normalised image is in finally taken to be the final surface density map of the field.

Appendix B: Spectroscopic catalogues of RXCJ 0014.3-3022 (A2744) and RXCJ 2308.3-0211 (A2537)

The full catalogue of non-stellar spectroscopic objects in the regions of the observed clusters is available at the CDS. Along with position and redshift, for each object we also provide the values of spectral indices and *BVR* magnitudes with their corresponding errors. Where equivalent widths were not calculated due to the line not being sampled in the instrument's spectral range, the table reads ND, i.e. Not Detected.

References

- Abraham, R. G., Smecker-Hane, T. A., Hutchings, J. B., et al. 1996, *ApJ*, 471, 694
- Adami, C., Mazure, A., Biviano, A., Katgert, P., & Rhee, G. 1998, *A&A*, 331, 493
- Alcalá, J. M., Pannella, M., Puddu, E., et al. 2004, *A&A*, 428, 339
- Arnouts, S., Vandame, B., Benoist, C., et al. 2001, *A&A*, 379, 740
- Baade, D., Meisenheimer, K., Iwert, O., et al. 1999, *The Messenger*, 95, 15
- Balogh, M. L., Morris, S. L., Yee, H. K. C., Carlberg, R. G., & Ellingson, E. 1997, *ApJ*, 488, 75
- Balogh, M. L., Morris, S. L., Yee, H. K. C., Carlberg, R. G., & Ellingson, E. 1999, *ApJ*, 527, 54
- Barger, A. J., Aragón-Salamanca, A., Ellis, R. S., et al. 1996, *MNRAS*, 279, 1
- Beers, T. C., Flynn, K., & Gebhardt, K. 1990, *AJ*, 100, 32
- Bertin, E., & Arnouts, S. 1996, *A&A*, 117, 393
- Biviano, A., Girardi, M., Giuricin, G., Mardirossian, F., & Mezzetti, M. 1992, *ApJ*, 396, 35
- Biviano, A., Metcalfe, L., McBreen, B., et al. 2004, *A&A*, 425, 33
- Biviano, A., Murante, G., Borgani, S., et al. 2006, *A&A*, 456, 23
- Böhringer, H., Schuecker, P., Guzzo, L., et al. 2001a, *A&A*, 369, 826
- Böhringer, H., Schuecker, P., Lynam, P., et al. 2001b, *The Messenger*, 106, 24
- Böhringer, H., Schuecker, P., Guzzo, L., et al. 2004, *A&A*, 425, 367
- Böhringer, H., Braglia, F., Pierini, D., et al. 2006, *The Messenger*, 123, 49
- Böhringer, H., Schuecker, P., Pratt, G. W., et al. 2007, *A&A*, 469, 363
- Bohlin, R. C., Jenkins, E. B., Spitzer, L., Jr., et al. 1983, *ApJS*, 51, 277
- Bolzonella, M., Pelló, R., & Miralles, J. M. 2000, *A&A*, 363, 476
- Boschin, W., Girardi, M., Spolaor, R., & Barrena, R. 2006, *A&A*, 449, 461
- Braglia, F., Pierini, D., & Böhringer, H. 2007, *A&A*, 470, 425 (BPP07)
- Butcher, H., & Oemler, A., Jr. 1978a, *ApJ*, 219, 18
- Butcher, H., & Oemler, A., Jr. 1978b, *ApJ*, 226, 559
- Butcher, H., & Oemler, A., Jr. 1984, *ApJ*, 285, 426
- Coia, D., McBreen, B., Metcalfe, L., et al. 2005, *A&A*, 431, 433
- Colberg, J. M., White, S. D. M., Jenkins, A., & Pearce, F. R. 1999, *MNRAS*, 308, 593
- Couch, W. J., Barger, A. J., Smail, I., Ellis, R. S., & Sharples, R. M. 1998, *ApJ*, 497, 188
- Cowie, L. L., Songaila, A., & Barger, A. J. 1999, *AJ*, 118, 603
- Dahle, H., Kaiser, N., Irgens, R. J., Lilje, P. B., & Maddox, S. J. *ApJS*, 139, 313
- Danese, L., de Zotti, G., & di Tullio, G. 1980, *A&A*, 82, 322
- Davis, M., Huchra, J., Latham, D. W., & Tonry, J. 1982, *ApJ*, 253, 423
- den Hartog, R., & Katgert, P. 1996, *MNRAS*, 279, 349
- Dietrich, J. P., Schneider, P., Clowe, D., Romano-Díaz, E., & Kerp, J. 2005, *A&A*, 440, 453
- Dressler, A. 1980, *ApJ*, 236, 351
- Dressler, A., & Gunn, J. E. 1983, *ApJ*, 270, 7
- Dressler, A., & Shectman, S. A. 1988, *AJ*, 95, 985
- Dressler, A., Oemler, A., Jr., Couch, W. J., et al. 1997, *ApJ*, 490, 577
- Dressler, A., Smail, I., Poggianti, B. M., et al. 1999, *ApJS*, 122, 51

- Durret, F., Lima Neto, G. B., Forman, W., & Churazov, E. 2003, *A&A*, 403, L29
- Ebeling, H., Barrett, E., & Donovan, D. 2004, *ApJ*, 609, L49
- Fadda, D., Biviano, A., Marleau, F. R., Storrie-Lombardi, L. J., & Durret, F. 2008, *ApJ*, 672, L9
- Fasano, G., & Franceschini, A. 1987, *MNRAS*, 225, 155
- Gavazzi, G., & Scodreggio, M. 1996, *A&A*, 312, L29
- Gavazzi, G., Pierini, D., & Boselli, A. 1996, *A&A*, 312, 397
- Girardi, M., Biviano, A., Giuricin, G., Mardirossian, F., & Mezzetti, M. 1993, *ApJ*, 404, 38
- Girardi, M., Giuricin, G., Mardirossian, F., Mezzetti, M., & Boschin, W. 1998, *ApJ*, 505, 74
- Gregory, S. A., & Thompson, L. A. 1978, *ApJ*, 222, 784
- Gunn, J. E., & Gott, J. R., III 1972, *ApJ*, 176, 1
- Halkola, A., Seitz, S., & Pannella, M. 2007, *ApJ*, 656, 739
- Horne, K. 1986, *PASP*, 98, 609
- Jones, C., & Forman, W. 1992, in *Clusters and superclusters of galaxies*, ed. A. C. Fabian, NATO ASI Series, 366, 49
- Katgert, P., Biviano, A., & Mazure, A. 2004, *ApJ*, 600, 675
- Kempner, J. C., & David, L. 2004, *MNRAS*, 349, 385
- Kodama, T., Smail, I., Nakata, F., Okamura, S., & Bower, R. G. 2001, *ApJ*, 562, L9
- Kodama, T., Smail, I., Nakata, F., Okamura, S., & Bower, R. G. 2003, *ApJ*, 591, 169
- Kron, R. G. 1980, *ApJS*, 43, 305
- Kull, A., & Böhringer, H. 1999, *A&A*, 341, 23
- Landolt, A. U. 1992, *AJ*, 104, 340
- Le Fèvre, O., Vettolani, G., Garilli, B., et al. 2005, *A&A*, 439, 845
- Lidman, C., Rosati, P., Tanaka, M., et al. 2008 [[arXiv:0808.2824](https://arxiv.org/abs/0808.2824)]
- Lilly, S. J., Le Fèvre, O., Hammer, F., & Crampton, D. 1996, *ApJ*, 460, L1
- Loh, Y., Ellingson, E., Yee, H. K. C., et al. 2008, *ApJ*, 680, 214
- Metcalfe, L., Fadda, M., & Biviano, A. 2005, *SSRv*, 119, 425
- McCracken, H. J., Radovich, M., Bertin, E., et al. 2003, *A&A*, 410, 17
- Mignano, A., Miralles, J.-M., da Costa, L., et al. 2007, *A&A*, 466, 541
- Moore, B., Katz, N., Lake, G., Dressler, A., & Oemler, A., Jr. 1996, *Nature*, 379, 613
- Moore, B., Lake, G., & Katz, N. 1998, *ApJ*, 495, 139
- Moore, B., Lake, G., Quinn, T., & Stadel, J. 1999, *MNRAS*, 304, 465
- Moran, S. M., Ellis, R. S., Treu, T., et al. 2007, *ApJ*, 671, 1503
- Morris, S. L., Hutchings, J. B., Carlberg, R. G., et al. 1998, *ApJ*, 507, 84
- Peacock, J. A. 1983, *MNRAS*, 202, 615
- Pierini, D., Zibetti, S., Braglia, F., et al. 2008, *A&A*, 483, 727
- Poggianti, B. M., Smail, I., Dressler, A., et al. 1999, *ApJ*, 518, 576
- Poggianti, B. M., von der Linden, A., De Lucia, G., et al. 2006, *ApJ*, 642, 188
- Porter, S. C., & Raychaudhury, S. 2007, *MNRAS*, 375, 1409
- Porter, S. C., Raychaudhury, S., Pimblett, K. A., & Drinkwater, M. J. 2008, [[arXiv:0804.4177](https://arxiv.org/abs/0804.4177)]
- Quilis, V., Moore, B., & Bower, R. 2000, *Science*, 288, 1617
- Renzini, A., & da Costa, L. 1997, *The Messenger*, 87, 23
- Robin, A. C., Reylé, C., Derrière, S., & Picaud, S. 2003, *A&A*, 409, 523
- Saintonge, A., Tran, K. V. H., & Holden, B. P. 2008, *ApJ*, 685, L113
- Scharf, C., Donahue, M., Voit, G. M., Rosati, P., & Postman, M. 2000, *ApJ*, 528, L73
- Schechter, P. 1976, *ApJ*, 203, 297
- Schlegel, D. J., Finkbeiner, D. P., & Davis, M. 1998, *ApJ*, 500, 525
- Scodreggio, M., Franzetti, P., Garilli, B., et al. 2005, *PASP*, 117, 1284
- Selman, F. J. 2004, in *Optimizing Scientific Return for Astronomy through Information Technologies*, ed. P. J. Quinn, & A. Bridger, *SPIE*, 5493, 453
- Tanaka, M., Finoguenov, A., Kodama, T., et al. 2008, *A&A*, 489, 571
- Tonnesen, S., & Bryan, G. L. 2008 [[arXiv:0808.0007](https://arxiv.org/abs/0808.0007)]
- Tran, K.-V. H., van Dokkum, P., Illingworth, G. D., et al. 2005, *ApJ*, 619, 134
- Vandame, B. 2004, Ph.D. Thesis, University of Nice-Sophia Antipolis
- Verdugo, M., Ziegler, B. L., & Gerken, B. 2008, *A&A*, 486, 9
- Whitmore, B. C., Gilmore, D., & Jones, C. 1993, *ApJ*, 407, 489
- Wilman, D. J., Pierini, D., Tyler, K., et al. 2008, *ApJ*, 680, 1009
- Zappacosta, L., Mannucci, F., Maiolino, R., et al. 2002, *A&A*, 394, 7
- Zhang, Y.-Y., Böhringer, H., Finoguenov, A., et al. 2006, *A&A*, 456, 55